# Fractal and compact growth morphologies in phase transitions with diffusion transport

T. Ihle and H. Müller-Krumbhaar
*Institut für Festkörperforschung, Forschungszentrum Jülich, D-52425 Jülich, Germany*
(Received 24 September 1993)

First-order phase transitions take place when a supercritical nucleus of the new phase grows into the old phase. A conserved quantity typically is transported through the old phase by diffusion. A recent theory has made quantitative predictions about a morphology diagram which classifies the various resulting patterns formed by the growing nucleus at long times. In this paper we present detailed numerical studies on the advancement of an interface due to diffusional transport. Important control parameters are the supercooling and the crystalline anisotropy. We confirm the basic predictions for the occurrence of the growth forms *compact* and *fractal dendrites* for anisotropic surface tension and *compact* and *fractal seaweed* for vanishing anisotropy. More specifically, we find the following results. For arbitrary driving forces an average interface can move at constant growth rate even with fully isotropic surface tension. At zero anisotropy and small driving force we find fractal seaweed with a fractal dimension $\approx 1.7$, in agreement with simple Laplacian aggregation. With increasing anisotropy the pattern can be described as fractal dendritic, growing faster than a compact dendrite, which finally is obtained at larger anisotropy. This is in agreement with the prediction for noisy dendrites. At large driving forces, but still below unit supercooling, we find a transition from the compact dendritic to a compact seaweed morphology when anisotropy is reduced as predicted. The transition appears to be discontinuous with metastable states. Symmetry-broken double fingers of the growing phase seem to be the basic building blocks for the compact-seaweed morphology.

PACS number(s): 61.50.Cj, 05.70.Fh, 68.70.+w, 81.30.Fb

## I. INTRODUCTION

Pattern formation in nonequilibrium systems [1,2] typically occurs when two possible phases of a system are driven out of coexistence so that one of the phases grows at the expense of the other phase. Implicitly it is assumed here that the two phases do not mix perfectly but are separated by an interface which moves during the growth. Some of the basic questions one would like to answer in this context concern the kind of structures that can be formed by such an advancing interface and how the structures and the conditions under which they are formed can be characterized.

The growth of a crystal from the melt or from a solution is a typical example for such a pattern forming process. This type of phase change usually requires the transport of at least one conserved quantity, the solute material or the latent heat of solidification, which is transported via diffusion. This is about the simplest pattern-forming process conceivable under essentially homogeneous nonequilibrium conditions. Mathematically this is known under the name *Stefan* [3] or *moving boundary* problem. Surprisingly enough it is still rather unclear what happens for long times in the limit of vanishing crystalline anisotropy, which corresponds to the case of a liquid droplet of some composition nucleating from a mixture of two liquids, if one ignores convective effects for the moment.

It has been known for about three decades [4] that such a growing nucleus becomes unstable as its radius becomes larger than a few times the critical radius. If the surface tension is anisotropic, for example, due to crystalline anisotropy, it is generally believed that the nucleus finally deforms into a dendritic pattern like a snowflake [2,5]. The limit of vanishing anisotropy, however, is much less clear.

There has been a recent attempt to formulate a theory [6,7] for the fundamental morphologies and the most relevant parameters controlling their appearance. This was based on scaling relations together with asymptotic matching requirements so that solutions expected in some limits of the parameters would be recovered. The resulting morphology diagram (Fig. 1) [7] uses *supercooling vs anisotropy* as the principal axes and discriminates between seaweed and dendrites as the basic patterns, where the dendritic patterns are characteristic for anisotropic growth conditions. A second classification concerns the patterns internal structures namely fractal as opposed to compact patterns. A fractal pattern is one with a self-similar or self-affine internal structure with a scaling range of at least one order of magnitude in length scales. The fractal region in parameter space is similar to the critical region in critical phenomena and accordingly a similar change over to the nonfractal compact region may occur without any singularity. Some basic predictions of this theory [7] can be summarized as follows.

The crystalline anisotropy in all cases considered here is assumed to be sufficiently small and nonsingular so that the crystal will not exhibit facets. This is often the case in organic crystals such as succinonitrile [8] or in liquid crystals [9–11] such as hexaoctyloxytriphenylene. For typical experimental situations the compact dendritic growth morphology then is the most likely one to occur. We will further assume that the anisotropy parameter

 

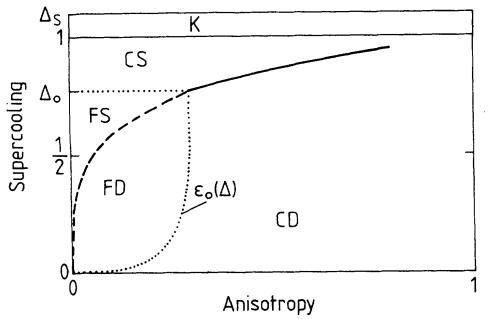


FIG. 1. Schematic morphology diagram supercooling $\Delta$ vs anisotropy $\epsilon_4$ for the compact and fractal, dendrite and seaweed growth patterns CD, CS, FD, and FS. The region surrounded by the dotted line depends on the noise. The region $K$ with supercooling $\Delta > 1$ is controlled by kinetics.

could be experimentally controlled. A reduction of this crystalline anisotropy should lead to different structures depending on the value of the supercooling which is the driving force for the interface motion.

At very large supercoolings but still with diffusion controlling the growth rate, the dendritic pattern is rather compact. This dendritic pattern was predicted to compete at low anisotropies with a compact-seaweed growth mode which should still grow at a nonzero velocity even when the anisotropy has completely vanished. In this limit of course the dendritic growth rate was predicted [12–15] and numerically confirmed [16,17] to go to zero. The compact-seaweed growth mode was conjectured to be an independent growth mode already several years ago under the name "dense branching morphology" [18]. There was no indication, however, that this could be discriminated from the compact dendritic mode in any qualitative way and it could have been just a completely smooth change of length scales. Some evidence for the occurrence of a real transition was gained by computer simulations of an Ising-like model [19]. In a short version [17] of our present investigation the first "proof" (at least numerically) was given for the existence of the compact-seaweed mode as a second mode of growth which for small anisotropy moves faster than dendrites and still moves at nonzero velocity in the isotropic case. This supports the theory [7] that the transition from compact dendritic to compact-seaweed growth under reduction of anisotropy is a nonequilibrium phase transition, and most likely of discontinuous nature.

At the typical low supercoolings used in most experiments and at sufficiently strong noise the dendritic structures furthermore were predicted to break up into fractal dendrites [7] similarly as was found to occur in Laplacian growth [20] and for vanishing anisotropy finally into fractal seaweed. Its fractal dimension was expected to be equal to the one obtained in atomistic simulations [21] of the Laplace aggregation. This behavior is also confirmed [17] by the present investigation concerning both the fractal dimension of the seaweed and the scaling of the growth rate depending upon supercooling. The approach to this limit should be sensitive to noise. This was investigated recently [22] and the results were found to agree with previous scaling predictions concerning the stability of dendrites and the appearance of fractal dendrites. The also predicted noisy discontinuous transition between compact and fractal seaweed at vanishing anisotropy so far could not be clearly identified because of the difficulty to precisely control the numerical noise.

In the present paper we give a somewhat detailed description of the numerical methods introduced for these investigations and we give the full details of the simulation results in comparison with existing theories and with some experiments. The paper is organized as follows. In Sec. II we shortly introduce the standard model of diffusional growth known as the Stefan problem of a moving interface. In Sec. III we describe the numerical scheme of a rotated-lattice sandwich which efficiently suppresses artificial numerical anisotropies under preservation of vectorizable codes. In Sec. IV we discuss the stability of dendrites and the influence of noise on dendritic growth and in particular the appearance of fractal dendrites. In Sec. V we present the results for fractal seaweed. In Sec. VI our results for compact seaweed at low and zero anisotropy are presented. In particular we compare these findings with results for growth in a channel and we discuss the predicted transitions to free dendritic growth and to the fractal seaweed morphology. A summary and outlook finally is given in Sec. VII.

## II. THE MOVING BOUNDARY PROBLEM

The system considered as an example is a crystal growing into its undercooled melt [2,14,5], where the growth is controlled by the diffusion of the latent heat of freezing. The diffusion field $u$ denotes the temperature difference measured from the value far away from the interface and normalized by the temperature increase due to the latent heat production. It obeys the diffusion equation

$$\frac{\partial u}{\partial t} = D\nabla^2 u \ , \tag{1}$$

with $D$ being the thermal diffusivity. When the crystal is growing with a velocity $v$, the latent heat produced at the solidification front should be transported away by the heat flow. The conservation law for energy then is written as

$$v_n = -D\mathbf{n}\cdot\nabla u \ , \tag{2}$$

with $\mathbf{n}$ being the normal vector of the interface. For simplicity we use here only the so-called one-sided model [14,5] with diffusion taking place on the "liquid" side of the interface only. A generalization with our numerical scheme discussed below is straightforward.

A rough nonfaceted interface can be regarded as being in local equilibrium. The diffusion field $u_i$ at the interface with curvature $\kappa$ then must fulfill the boundary condition

$$u_i = \Delta - d\kappa \ . \tag{3}$$

Here $\Delta$ is the dimensionless undercooling and $d$ is an anisotropic capillary length with a fourfold symmetry as

$$d(\theta) = d_0(1-\epsilon_4\cos 4\theta) \ . \tag{4}$$

In the absence of surface tension, i.e., $d_0=0$, Ivantsov [23] showed that a parabolic needle crystal may grow steadily with a tip radius $\rho$. The undercooling $\Delta$ determines the product of $\rho$ and the growth velocity $v$, or the Péclet number $p \equiv v\rho/2D$. In two dimensions, for example, the relation is [23]

$$\Delta = 2\sqrt{p}\, e^p \int_{\sqrt{p}}^{\infty} dx \exp(-x^2) . \tag{5}$$

Relation (5), however, cannot determine the growth rate uniquely for a given $\Delta$ since there are infinite combinations of $v$ and $\rho$ possible for a given product $p$. Furthermore, all Ivantsov parabolas were found to be unstable [24] against small perturbations. It was later shown [12–15] that interface tension together with a nonzero anisotropy $\epsilon_4$ is necessary to stabilize a unique Ivantsov parabola against infinitesimal perturbations. The growth rate $v$ satisfies a universal scaling relation

$$v d_0/2Dp^2 = \sigma(\epsilon_4) . \tag{6}$$

Here $\sigma$ depends only on the anisotropy of the surface tension $\epsilon_4$, but is independent of the dimensionless undercooling $\Delta$. The scaling relation (6) has been confirmed by previous numerical simulations [16].

A completely unsolved problem so far has been the evolution of an initially flat interface with fully isotropic surface tension. Clearly, if the interface remains flat, stationary growth at a constant growth rate is only possible when the supercooling is precisely unity (ignoring the possibility of interface kinetics for the moment). This is an immediate consequence of the conservation law responsible for the diffusion equation. Alternatively, for a perfectly flat interface the growth rate must go to zero at long times for $\Delta < 1$.

To escape from this strict condition one must give up the assumption of a flat interface. As shown by Mullins and Sekerka [4], a flat interface is linearly unstable against large wavelength perturbations. The fastest growing mode has a wavelength of the order of the Mullins-Sekerka or stability length $\rho_{\mathrm{MS}}$,

$$\rho_{\mathrm{MS}} = 2\pi\sqrt{d_0 l_D} , \tag{7}$$

with $l_D = 2D/v$ being the diffusion length and $v$ the velocity of the front. Therefore assume that the solid-liquid interface deforms into a fingery or comblike structure with grooves which become deeper in growth direction as time goes on. One may then define an *envelope* over the front of this complex structure, calling this suitably averaged envelope the *average* interface in contrast to the *local* interface separating the solid from the liquid. This average interface can be considered as the real growth front in the sense that it is not just a solid that grows from the liquid (in our present picture) but in fact a two-phase mixture solid plus liquid grows into a one-phase region originally consisting of liquid only. With a properly adjusted fraction of liquid in the mixed-phase region one can easily define an averaged supercooling so that no long-range diffusional transport into the far liquid is needed anymore. In this way it becomes conceivable that the system adjusts itself to an effective unit supercooling of the mixed phase so that a constant growth rate of the averaged front becomes possible at long times. It is a central point of the present investigation to show that this growth mode is possible and to elucidate its details.

## III. THE ROTATED-LATTICE SANDWICH

A basic problem in every large-scale numerical project is that the relevant length scales and time scales must be clearly separated and identifiable in order to achieve trustworthy results. This condition implies that one must have some *a priori* estimates on what these scales could be. In our case it is fairly clear that we have to separate at least the length scales of the dendritic tip radius, the stability length, and the diffusion length. Note that the order of magnitude of these scales may depend on parameters. In principle also the capillary length enters but practically only via the stability length. Separating these three length scales requires about $10^3$ units of the numerical grid in every direction. Concerning the time scales it is clear that a vectorizable method of computation is highly desirable as time scales in diffusion problems scale as $L^{2+d}$, with $L$ being the linear grid size and $d$ the space dimension. Our computational method was specifically designed to meet these requirements.

A straightforward numerical treatment for the Stefan problem using a computational grid for the diffusion equation automatically introduces some artificial anisotropy, even if $\epsilon_4=0$ in (4). Although this anisotropy is very small, it causes problems because the developing shape of the interface is very sensitive to anisotropy. The basic idea for a controlled reduction of this undesirable anisotropy at high computational speed on vector computers is to use a stack of two or more grids which are rotated and shifted against each other, and to average over them (Fig. 2). Admittedly, the procedure described in the following is somewhat tedious to implement. We felt, however, that this effort is necessary in order to obtain reliable results with percent precision.

All previous attempts to numerically treat this morphology problem were hampered in one or the other way by this anisotropy or by system size or computing-time

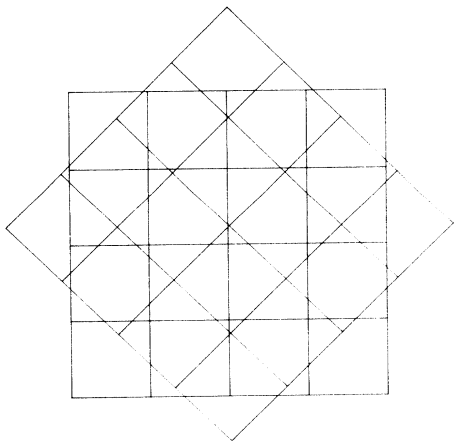

FIG. 2. The rotated-lattice sandwich with two square grids rotated by an angle of $\pi/4$ against each other.

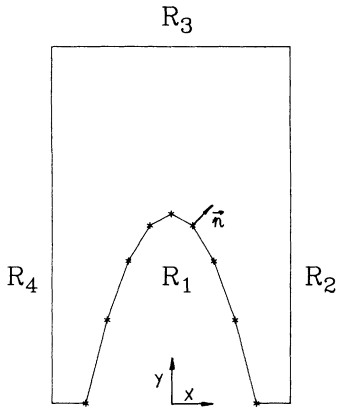


FIG. 3. The computational frame with the moving solid-liquid boundary $R_1$ and three walls $R_2$, $R_3$, and $R_4$.

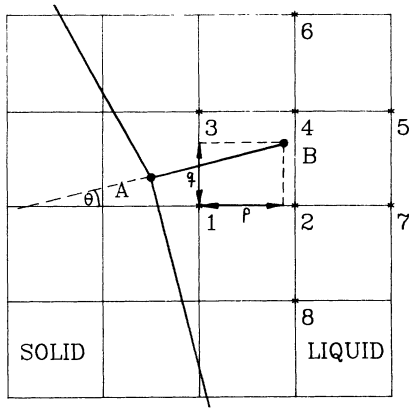


FIG. 4. Calculation of the gradient of the diffusion field at the interface point $A$ by means of a special eight-point interpolation using the grid points 1–8.

requirements. The lattice models without rotation [25,19,26] have the problem of anisotropy and when they are atomistic, of strong noise, phase-field models [27,28] need an additional length scale for the interface thickness and introduce a kinetic coefficient, fully time-dependent Green's-function representations [29] for complex morphologies do not seem to be easier to implement efficiently.

First we define an outer frame (Fig. 3) which consists of a channel formed by two rigid sidewalls $R_2$ and $R_4$. Across the channel lies the moving boundary $R_1$, which is discretized and which may be deformed. The "far" boundary $R_3$ is kept straight but mobile. Then we map this frame onto a number of two or more independent regular grids which are shifted by irrational amounts and rotated against each other. Most of the simulations were performed on a stack of four lattices rotated by a fixed angle of $\pi/8$ against each other leaving no four- or eight-fold anisotropy. Even higher-order anisotropy was not detected within our numerical accuracy.

The discretized diffusion field $u$ is defined at the grid points inside the frame. In the following we denote the inside of the frame as liquid and the outside as solid, specifically the part across boundary $R_1$.

The numerical simulation is performed as follows. First an initial shape of the moving boundary is chosen. In most cases we take an Ivantsov-parabola as shown in Fig. 3, because we know the exact value of the diffusion field for vanishing capillary length. With this Ivantsov solution we initialize the different diffusion grids. By means of the interface points which form the moving boundary $R_1$ (Fig. 3) we calculate the normal vector, the local curvature, and the boundary condition (3) at each of these points. The interface points are thought to be connected with straight lines and the boundary conditions on them are linearly interpolated from the nearest-neighbor points.

At each point of the interface we have to determine the normal velocity (2), which is proportional to the gradient of the diffusion field in normal direction. Since the interface can be very complicated and can be located between grid points an interpolation is necessary. To do this, we place a point $B$ (Fig. 4) a fixed distance $\sqrt{2}+\varepsilon$ apart from the considered interface point $A$ into the liquid. The small shift $\varepsilon$ is necessary to ensure that in any case all grid points needed for the interpolation are in the liquid.

As a general rule for interpolations with a varying number of anchor points which we encounter here we tried to make sure that no jump discontinuities occur as the interface advances. The value of the diffusion field and its derivatives in the $x$ and $y$ directions at this point $B$ are obtained by a special eight-point interpolation, which is exact in second-order, symmetrized and insensitive to changes of the angle $\theta$ (Fig. 4). Explicitly the diffusion field at the point $B$ is approximated by

$$
\begin{aligned}
u_B = W(\theta)\Big\{ & u_1(1-p)(1-q)+u_2\frac{(1-q)(2p-q)}{2}+u_3\frac{(1-p)(2q-p)}{2} \\
& +u_4(p+q+pq-p^2-q^2)+u_5\frac{p(p-1)}{2}+u_6\frac{q(q-1)}{2}\Big\} \\
+[1-W(\theta)]\Big\{ & u_1\frac{q(q-1)}{2}+u_2(2p+q-pq-p^2-q^2)+u_3q(1-p) \\
& +u_4\frac{q(q-1+2p)}{2}+u_7\frac{p(p-1)}{2}+u_8\frac{q(q-1)}{2}\Big\} .
\end{aligned}
\tag{8}
$$

In the special case of Fig. 4 with $-\pi/4 \leq \theta \leq \pi/4$ the weight $W(\theta)$ is equal to $1/2+\sin(\theta)/\sqrt{2}$. The formulas for the derivatives can be easily derived from this equation. Since the value of $u$ at the interface point $A$ is known from the boundary condition (3), we can now approximate the $u$ field between the points $A$ and $B$ to second order in the distance from $B$. The gradient at the point $A$ multiplied by $-D$ yields a second-order approximation for the local normal velocity.

It turned out that this complicated treatment is necessary because a linear interpolation introduces too large errors. A linear approximation which needs only four points in the liquid is used in special cases when not all eight grid points are available, i.e., when one of these points is situated in the "solid." This situation can occur in very narrow troughs. If a trough is so small that even the linear approach fails, the local velocity is set to zero. It follows from this procedure that the numerics cannot produce reliable troughs narrower than $2\sqrt{2}+\varepsilon$ grid units. Even in this limit the procedure turned out to be rather robust against selfintersection of the moving boundary.

For further improvement and noise reduction we use a boundary element method to calculate the normal velocity. This method uses the maximum information available about the diffusion field $u$ in the surrounding of the interface. Figure 5 shows a small part of the moving boundary with three interface points $i-1$, $i$, and $i+1$ and two curve segments $K_1$ and $K_2$. In order to calculate the velocity at the point $i$ the two segments $K_1$ and $K_2$ are cut into $2N$ parts. $N$ is typically set around three. We calculate the normal velocities at these new interface points by means of the method described above. The average of the velocities $a_1, \ldots, a_4$ (Fig. 5) is given by $a_l$ ($l$ meaning left), the average of $a_5, \ldots, a_8$ is given by $a_r$ ($r$ meaning right). Now imagine that the left segment $K_1$ is shifted parallel by the distance $a_l \Delta t$ and the right segment $K_2$ by $a_r \Delta t$. These two shifted segments hit the normal vector of the point $i$ at two points close together. These points are averaged and the distance $v_i \Delta t$ to the point $i$ gives the normal velocity $v_i$.

We now have to solve the diffusion equation on the grid obeying simultaneously the boundary conditions (3) on the moving boundary. The interface points are allowed to change smoothly, i.e., their positions are not restricted to the points of the diffusion grid. The boundary condition (3) is defined at these interface points which can lie between the grid points. We would like to incorporate this boundary condition directly into the diffusion field defined on the grid points in order to speed up the computation. For this purpose we extrapolate those grid-points which are situated directly behind the moving boundary in the solid from the known value at the interface (3) and the values of two points from inside the liquid. Despite the use of a total of three points this is a linear extrapolation along the grid lines. At some of the border points there are different possibilities to do this. As an example Fig. 6 shows an interface with five border points. There are three possibilities to determine the value of the point number 3 by extrapolation from the liquid side: two possibilities in the $y$ direction by means of the liquid points $A_1, A_2$ or $B_1, B_2$, respectively, and one possibility in the $x$ direction by means of $C_1$ and $C_2$. To ensure symmetry all three different results are averaged to obtain the local value at point 3. In numerical tests we received the best results when we assumed in this boundary procedure that the interface had already grown by $v_n \Delta t/2$, $\Delta t$ being the numerical time step and $v_n$ the local normal velocity calculated above.

A cross section through the interface is again sketched in Fig. 7, which shows in detail the extrapolation of the border point $(i-1,j)$ in the $x$ direction by means of the grid points $(i,j)$ and $(i+1,j)$. $x_0$ denotes the interface position at time $t+\Delta t/2$. A simple linear extrapolation which needs only the point $(i,j)$: $u_{i-1,j}=[u_0-(1-\delta)u_{i,j}]/\delta$ is not useful when $\delta \to 0$. Therefore we use a different linear extrapolation, taking into account the point $(i+1,j)$ and take the weighted average of the two possibilities. The two linear interpolation formulas are

$$u_s^a=\delta u_{i-1}+(1-\delta)u_i, \quad u_s^b=\frac{(1+\delta)u_{i-1}+(1-\delta)u_{i+1}}{2}.$$

The weighted average of these is

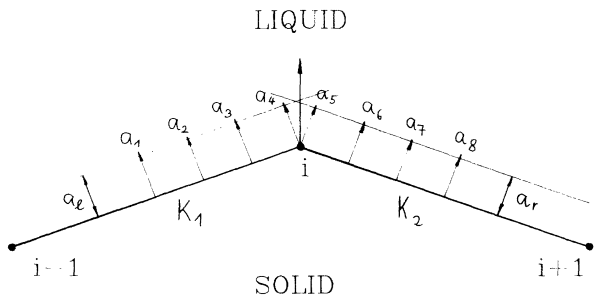


FIG. 5. Boundary element method for an improved velocity calculation. A part of the interface with the three points $i-1$, $i$, and $i+1$ is shown. The normal velocity of the point $i$ is to be determined.

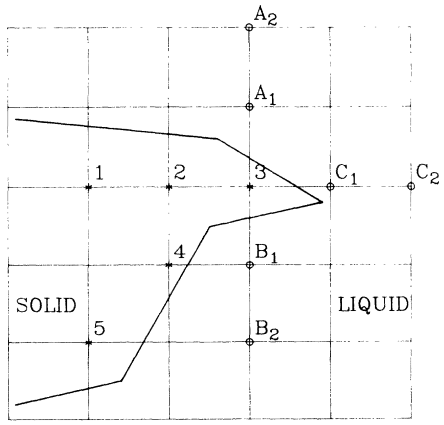


FIG. 6. Setting the boundary condition at the moving boundary. The five border points 1–5 are placed directly behind the boundary and their values are calculated by an extrapolation from points in the liquid.

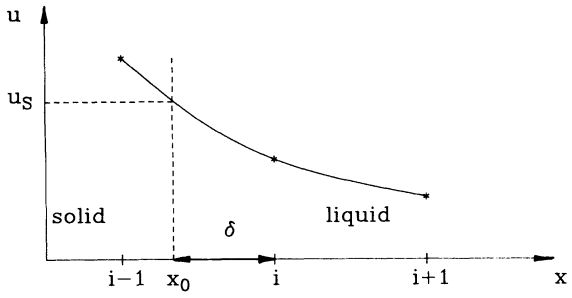


FIG. 7. Detailed schematic plot of the extrapolation of the border point $i-1$ by means of the points $x_0$, $i$, and $i+1$. At the interface position $x_0$ the diffusion field has the boundary value $u_S$.

$$u_s^* = \delta u_0^a + (1-\delta) u_0^b \ . \tag{9}$$

It follows that

$$u_{i-1}^* = \frac{u_s + \delta(1-\delta)u_i - (1-\delta)^2 u_{i+1}/2}{\delta^2 + (1-\delta^2)/2} \ . \tag{10}$$

This formula is numerically stable for $0 \le \delta \le 1$. Since the extrapolation needs at least two liquid points in the $x$ or $y$ direction it works in all those cases where the velocity procedure is applicable.

Next we must satisfy boundary conditions on the outer frame. For free growth simulations we used the same procedure described above but with the condition $u=0$ instead of (3). This causes no appreciable error as long as the interesting parts of the shape are several diffusion lengths away from the walls. The case of reflecting or periodic boundary conditions on the sidewalls of the frame will be described later.

We now have the diffusion field completely defined using the grid points only, i.e., we have already incorporated the boundary conditions at the interface. Note, however, that this applies only to the liquid; the $u$ values in the solid are only meaningful near the interface and for one time step. This incorporation of the boundary conditions was originally developed for the one-sided model, but it can be easily generalized into a two-sided model with different material properties on both sides of the interface at the expense of doubling the computing time.

Now we can perform a time step with the discretized diffusion equation

$$u_{i,j}^{n+1} = u_{i,j}^n + \frac{D\Delta t}{\Delta x^2}(u_{i+1,j}^n + u_{i-1,j}^n + u_{i,j+1}^n + u_{i,j-1}^n - 4u_{i,j}^n) \ . \tag{11}$$

As it is well known this explicit scheme is stable only if $\Delta t \le \Delta x^2/(4D)$. In our simulations at large normal velocities it turned out to be more effective to do from two up to five small time steps with this simple scheme rather than using a sophisticated implicit scheme with a larger time step. This can be understood by two arguments. First, there is a small time scale not much larger than the critical time step due to the possible change in the curvature of the interface even at small displacements. Second, the shape of the structure is very sensitive to breaking the symmetry between the $x$ and $y$ directions on the grid. Hence a powerful implicit scheme working with operator splitting must be symmetrized and also becomes time consuming. The maximum displacement of the interface $v_n \Delta t$ at each time step was lower than 0.1 grid units in all simulations. Therefore we used the implicit scheme mainly at low normal velocities.

Note that we have typically $N=4$ complete systems consisting of interfaces, outer frames, and diffusion fields, but the interfaces and frames are geometrically identical and differ only by rotation and translation. At each time step $\Delta t$ the determination of the local velocity of the interface, the incorporation of the boundary condition into the grid, and the diffusion step are performed independently on all $N$ grids and interfaces. We advance each interface by its own velocity and determine the average of all these interfaces. This is possible because the interfaces were geometrically identical before advancing. This averaged interface is then redistributed to the different grids by rotation and translation. Since this average is taken after each of the small time steps, the influence of the artificial anisotropy from the underlying lattice can be suppressed almost completely.

When the interface advances the distances between consecutive interface points may change because every interface point moves in normal direction with its own velocity. After each time step these distances are adjusted to fall in an interval $s_{\max}/2 < s_j < s_{\max}$. If the length of such a segment exceeds $s_{\max}$ a new point is added in the middle of an averaged arc. If two consecutive points come too close, one of them is eliminated. $s_{\max} = 2-3$ grid units seems to be a good choice. After the addition or elimination of points, all distances between the interface points are equilibrated by diffusing the points along the interface. The iteration is now repeated with this new interface. This procedure has been proved to be successful already in previous simulations by a Green's-function method [16].

During the simulation the foremost part of the structure was always kept approximately at the center of the grids. This makes long time runs possible and can be achieved as follows: After growing over some grid units the interface and the values of the diffusion field are shifted against the grid by the same amount. This takes place independently on all grids. The shift vectors have integer components in grid units. Therefore they do not cause interpolation errors. They are constructed in such a way that the foremost tip of the structure is always as close as possible to the center of each grid. After shifting the structure against the grid, some parts of it can lie outside the outer frame (Fig. 3). We cut off these parts which do not matter, if their distance to the foremost fingers is large enough. For the simulations in a channel we need reflecting boundary conditions at the sidewalls $R_2$ and $R_4$ in Fig. 3. This is done by setting the field on the grid points which are outside the computational frame but near these walls to special values. These values are calculated at each time step in such a way that the gradient of the diffusion field $u$ perpendicular to the sidewalls is zero.

It is of course beyond our computational power to reach the long-time limit of a completely free developing crystal. Therefore we tried to approach this situation by a system with periodic boundaries at the walls $R_2$ and $R_4$. This does not produce errors if all physical length scales are much smaller than the periodicity length. In contrast to the channel with reflecting boundaries the periodic boundary conditions allow for horizontal drifts without time limitation. It is particularly important to achieve exact translational invariance for these periodic boundary conditions in order to avoid pinning effects. While this is simple for a single lattice, simultaneous periodic boundary conditions with the same periodicity length $W$ on two or more rotated lattices are not rigorously possible for arbitrary angles of rotation.

Explicitly it is impossible to fulfill the conditions

$$W^2=a_i^2+b_i^2, \quad \alpha_i=\arctan\left[\frac{a_i}{b_i}\right] \tag{12}$$

for arbitrary angles $\alpha_i$ of rotation and integer numbers $a_i$ and $b_i$ for the lattice $i$ on more than one grid. Figure 8 shows a specific channel which satisfies the conditions (12). As a useful compromise we allowed the periodicity length to differ slightly from $W$ and the rotation angles to be not exactly equal to $\pi/4$ or $\pi/8$, respectively. Different periodicity on the lattices requires an additional dilation or contraction by redistributing the average interface to the different lattices. We have chosen specific numbers of grid units to further minimize the already small error. The conditions

$$\left|\alpha_i-\arctan\left[\frac{a_i}{b_i}\right]\right|\leq 0.01^\circ\,, \qquad \frac{|W-W_i|}{W}\leq 0.001 \tag{13}$$

are satisfied for many numbers above $W=277$ grid units, for instance, for $W=277,290,366,\ldots,478$. $W_i$ and $\alpha_i$ are the actually realized periodicity or angle, respectively, on grid $i$, while $W$ and $\alpha$ are the ideal values. These rational approximations for irrational relations introduce here relative errors of less than $10^{-3}$ or even $10^{-4}$, but maintain full translational invariance.

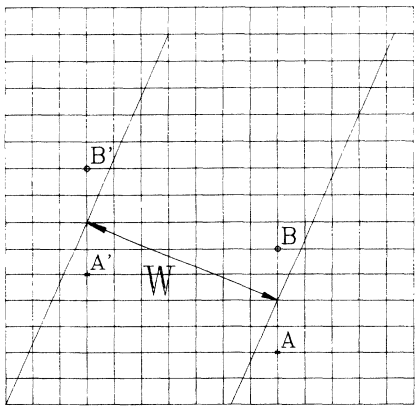


FIG. 8. Schematic plot of the periodic boundary condition. The rotation angle $\alpha$ is commensurable with $\tan(\alpha)=a/b=\frac{3}{7}$ and the width of the channel is $W=\sqrt{58}$. The point $A$ is equivalent to the point $A'$ and the point $B$ is equivalent to the point $B'$.

## IV. COMPACT DENDRITES AND FLUCTUATION EFFECTS

After numerous simple tests such as the growth of a flat and a circular interface we simulated dendrites and

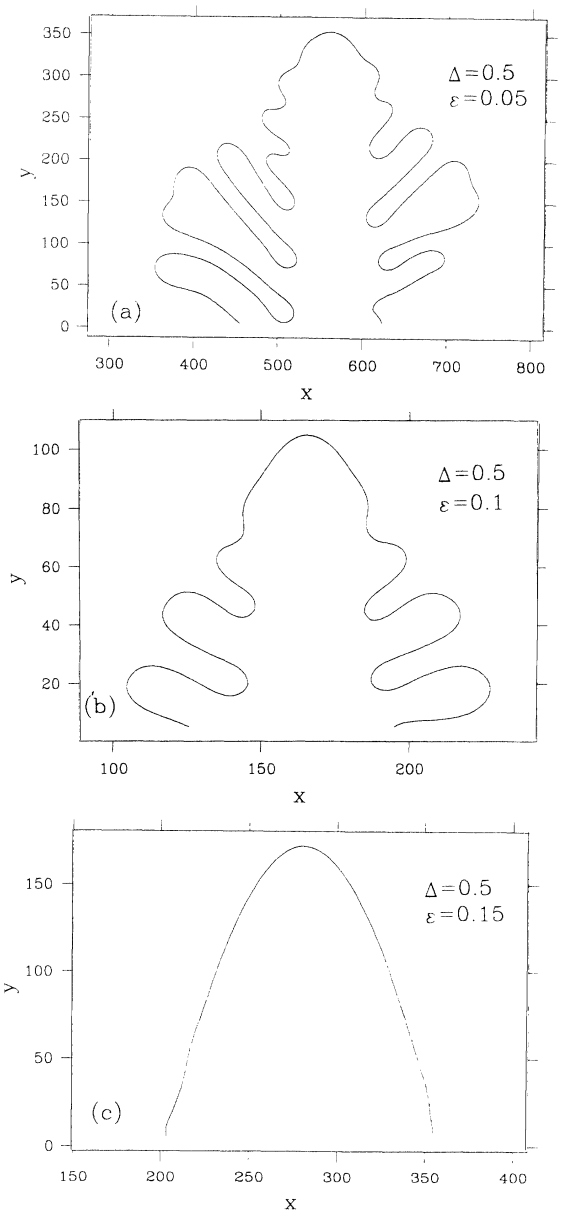


FIG. 9. Dendrite crystals grown from an initial Ivantsov parabola at different anisotropies simulated on a stack of four grids. The parameters were $D=1$, $\Delta=0.5$, (a) $\epsilon_4=0.05$, $d_0=0.075$, $l_D=139$, $R_{\rm tip}\approx 22.5$, lattice size $1121\times 1121$; (b) $\epsilon_4=0.1$, $d_0=0.05$, $l_D=45.5$, $R_{\rm tip}\approx 8.7$, lattice size $333\times 333$; and (c) $\epsilon_4=0.15$, $d_0=0.17$, $l_D=87$, $R_{\rm tip}=15.53$, lattice size $561\times 561$. Here and in the following all lengths are given in lattice units of the computational grid $LU$, all times in $LU^2/D$, and all velocities in $D/LU$. The diffusion length $l_D$ was obtained in the stationary regime by $l_D=2D/V_{\rm tip}$.

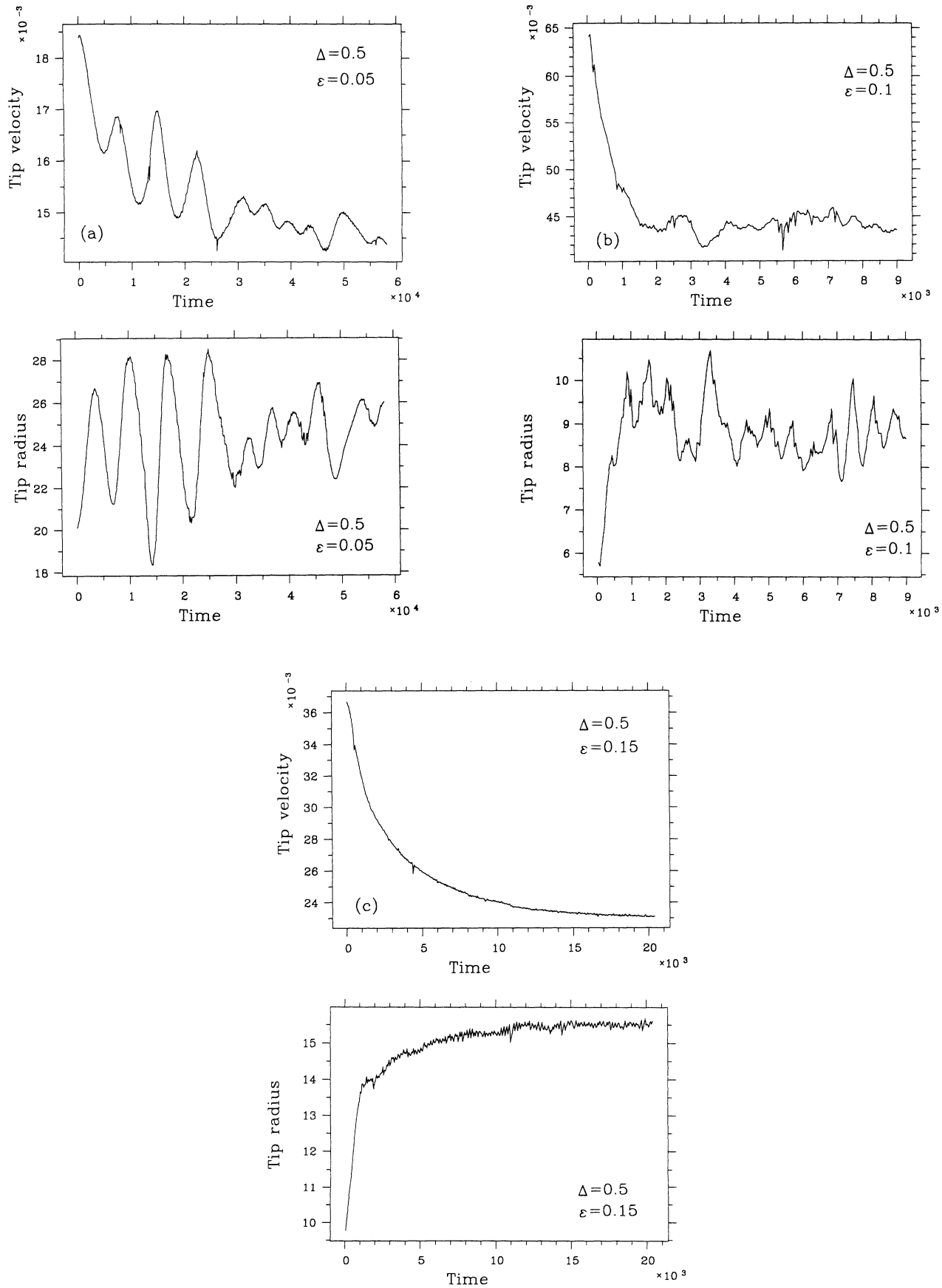


FIG. 10. Temporal variations of the tip radius and velocity of the dendrites shown in Fig. 9. As before the tip radius is given in lattice units of the computational grid $LU$, time in $LU^2/D$, and velocity in $D/LU$.

measured their tip velocities and radii in dependence on the anisotropy of the capillary length. The results were compared with accurate numerical results known from a (per definition) fully isotropic Green's-function calculation [16] in quasistationary approximation. Most of the simulations were performed with undercooling $\Delta$ between 0.5 and 0.8 and with fourfold anisotropy in the range $0.05 \leq \epsilon_4 \leq 0.2$. The tip radii were between 9 and 40 grid units. The largest distance $s_{\max}$ between consecutive interface points is 2 grid units. The initial configuration usually was an Ivantsov parabola growing with a higher velocity as expected for the stationary needle crystal.

The tip of the dendrites are automatically kept at a distance of at least two diffusion lengths from this outer frame in order to suppress boundary effects. If the tip of the dendrite grows too close to the far wall, the moving boundary and the values of the diffusion field are shifted backward by an integer number of grid units against the outer frame and the grid. Now the shifted dendrite exceeds the fixed frame and must be cut off at the bottom. Since the growth rate of the dendrite is primarily governed by the dendrite tip, only a very small error due to the cutoff in the tail region is supposed to occur.

Figure 9 shows three dendritic crystals in their stationary regime grown on four grids with different anisotropies $\epsilon_4 = 0.05$, 0.1, and 0.15 at an undercooling of $\Delta = 0.5$. In Fig. 10 the time evolution of the tip radius and velocity for these dendrites is shown. Note that there are almost no sidebranches for the dendrite with high anisotropy $\epsilon_4 = 0.15$, while the crystal with $\epsilon_4 = 0.05$ is near the instability region, which is indicated by the strongly irregular sidebranching and the large fluctuations in the tip radius and velocity. Figure 11 shows the normalized growth rate $\sigma = d_0 v/(2Dp^2)$, where $d_0$ is the capillary length and $p$ is the Péclet number, versus anisotropy for dendrites calculated on two and four grids and with the Green's-function method. The Péclet number $p$ in the definition of $\sigma$ is calculated for the given undercooling from the Ivantsov relation (5). The Péclet number $\tilde{p}$ obtained by calculating $VR/(2D)$ from the simulations is always slightly smaller than $p$ and depends on anisotropy in agreement with [16].

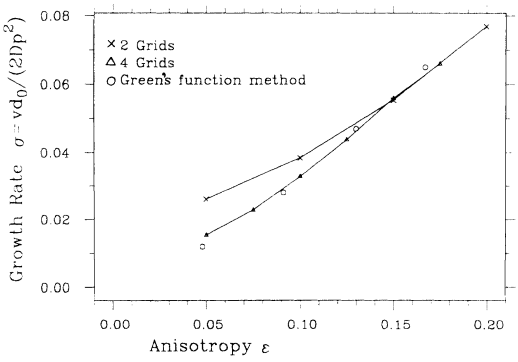


FIG. 11. The normalized growth rate $\sigma = vd_0/(2Dp^2)$ of dendrites is plotted vs anisotropy $\epsilon_4$. Data obtained by numerical simulation based on the Green's-function method [16] are plotted with ○. Data from our method are plotted with × for a calculation on two grids (angle 0, $\pi/4$) and with △ on four grids (angle 0, $\pi/8$, $\pi/4$, $3\pi/8$). Note the appreciable deviations of the two-grid simulation from the Green's-function method at low anisotropy which presumably is due to some rest of numerical anisotropy.

At low anisotropy the two-grid version yields growth rates twice as high as those of the Green's-function method while the four-grid version agrees within 20%. Thus most of the following simulations were done on a stack of four grids leaving no four- and eightfold numerical anisotropy. The wavelength of the sidebranches scales with the Mullins-Sekerka length (7) as $\lambda \approx 2.6\rho_{\mathrm{MS}}$, in agreement with previous simulations [16]. The CPU time for reaching the stationary dendritic solution lies between 18 min [dendrite in Fig. 9(b)] and 37 h [dendrite in Fig. 9(a)] on a CRAY-XMP supercomputer depending on the anisotropy and the degree of discretization. Thus the computational speed is comparable to that of the Green's-function method for the same resolution, although there is somewhat more noise produced by the present fully time dependent scheme.

After these initial tests we considered the range of stability of these primary dendrites. The stationary state of a needle crystal growing at nonzero anisotropy resembles very closely a parabola [14]. Without anisotropy no stationary needle crystal symmetrical about the tip is possible [12–15]. Using numerical methods similar to [24] it was found [30] that only the fastest growing solution from the discrete set of possible stationary needles was stable. Analytical results based on WKB-type approximations [31,32] gave the following picture for the dynamical stability.

We assume to be in a frame of reference moving along with the tip of the needle. A wave packet of deformation introduced a short distance away from the tip will grow in amplitude, spread, and will be driven towards the tail of the dendrite. This causes the sidebranches of the dendrite. Close to the tip region this looks like a convective instability: A perturbation in the laboratory frame will grow indefinitely, but in the moving frame it will decay. In fact, it was shown [33,31] that this is not quite correct as the amplitude of the sidebranches will not grow without bound, so the fastest growing needle will be completely stable. The possibly most rigorous analysis [14] states that the tip of the needle crystal is absolutely stable against small perturbations if they have only real eigenvalues in the stability spectrum. An alternative picture, however, was given recently. There it was argued [34] that the spreading rate of the wave packet might become so large that the tip could undergo strong oscillations or even become unstable. From the evolution of a wave packet traveling down the shaft of the dendrite it is obviously not easy to conclude rigorously what happens directly at the tip. This puzzle has its origin in the old argument [24] that the tip becomes unstable if its radius of curvature becomes significantly smaller than the stability length $\lambda_s = 2\pi\sqrt{2d_0D/v}$. This situation is encountered in the limit of small anisotropy $\epsilon_4$ or small $\sigma$ because of the relation $\lambda_s/\rho = 2\pi\sqrt{\sigma}$, which results from (6). Our conclusion here is in agreement with the general opinion [31,32,14] that the dendrite tip even in the limit

of very small but nonzero anisotropy remains linearly stable against arbitrary perturbations of infinitesimal amplitude. A recently given simple argument [22] illustrates our conclusion, Fig. 12. Assume that an almost parabolic needle crystal moves at velocity $v$. At small anisotropy with small $\sigma$ the stability length $\lambda_s$ is very much smaller than the tip radius $\rho$.

Assume now that we introduce a spatially oscillating perturbation of wavelength $\lambda \approx \lambda_s$ with infinitesimal amplitude over the tip region. According to the Mullins-Sekerka stability analysis of a flat plane [4] this perturbation grows with time $\sim \exp(\Omega t)$ and therefore tries to destabilize the tip. This argument, however, ignores the small but nonzero curvature of the tip. Since the motion of the crystal surface is always in normal direction, a point on the surface close to the tip will eventually be driven away from the tip, even though this is initially a very slow process for points very close to the tip, as illustrated in Fig. 12. A point originally at a small distance $x_0$ away from the tip is slowly moving down the shaft relative to the tip position due to convection. A short calculation [22] shows that within a time

$$\delta t \sim \frac{\rho}{v}\left[c_1+\ln\sqrt{2c_1}+\ln\left[\frac{\rho}{x_0}\right]\right] \tag{14}$$

the point has gone down the shaft by a distance $c_1\rho$, with $c_1$ being a constant of order unity. At this time the point on the interface has essentially left the tip region. Assume now that $x_0 \approx \lambda^*/4$ is the first node point of the perturbation of the most dangerous fastest growing mode with periodicity $\lambda^* = \sqrt{3}\lambda_s$ near the tip, where the amplitude of the perturbation changes its sign. If the amplitude initially is infinitesimal, it remains arbitrarily small during the time $\delta t$, but the node then has left the tip region. In other words, the perturbation has disappeared from the tip region. This explains why the dendrite tip is stable against infinitesimal perturbations since a perturbation, even when it is located directly at the tip, tends to be convected away.

If the initial amplitude of the perturbation exceeds a critical value of

$$A^* = \rho \exp\left\{-\frac{\pi}{3}\frac{\rho}{x_0}\left[c_1+\ln(\sqrt{2c_1})+\ln\left[\frac{\rho}{x_0}\right]\right]\right\}, \tag{15}$$

the perturbation becomes much larger than $\rho$ during the time $\delta t$ and the tip will split into finer structures. Hence the dendrite is absolutely unstable against this perturbation.

In Fig. 13 we plot $A^*/\rho$ logarithmically versus $\sigma = (8/3\pi)(x_0/\rho)^2$ with $c_1 = 1$. The dendrite tip accordingly is unstable against finite amplitude perturbations when the amplitude of the perturbations is larger than the critical value $A^*$. This tip analysis agrees in its basic scaling properties with the previous results [33,31] from the analysis of wave packets moving along the shaft. A similar consideration has been made before for the somewhat related Saffman-Taylor problem [35]. So far we considered the deterministic growth of an imposed perturbation. This process can be related to the perturbations generated by a noise source acting continuously on the tip [36,22]. This noise was introduced in Ref. [36] by adding at a point $\mathbf{r}_I$ near the tip a random Gaussian velocity $v^R$ to the systematic part of the velocity

$$v^R(\mathbf{r},t) = \gamma_0 \tilde{R}(t)\delta(\mathbf{r}-\mathbf{r}_I), \tag{16}$$

with $\langle \tilde{R}(t)\tilde{R}(t')\rangle = \delta(t-t')$ and $\gamma_0$ being the strength of the noise. This becomes equivalent to an initial deformation of the interface with amplitude

$$A \approx \frac{\gamma_0}{\sqrt{4\pi|\Omega''_{k^*}|}} \tag{17}$$

near the tip [22]. Here $\Omega''_{k^*}$ is the second derivative of the Mullins-Sekerka dispersion relation [4]

$$\Omega(k) \cong \frac{2Dk}{l_D}\{1-\tfrac{1}{2}d_0 l_D k^2\} \tag{18}$$

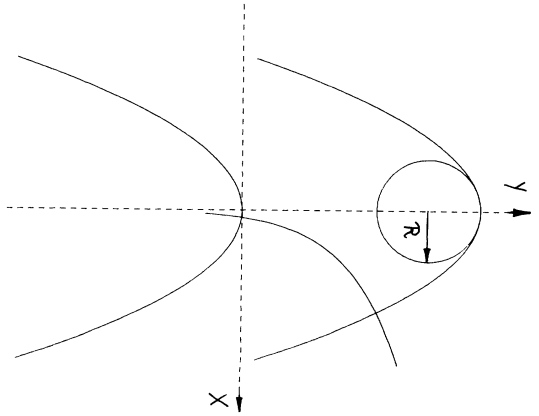


FIG. 12. Schematic plot of the convective motion of a nodal point on the surface of a parabolic dendrite, initially at position $x_0$. As time goes on, the nodal point moving in a normal direction to the parabolic surface is driven away from the tip.

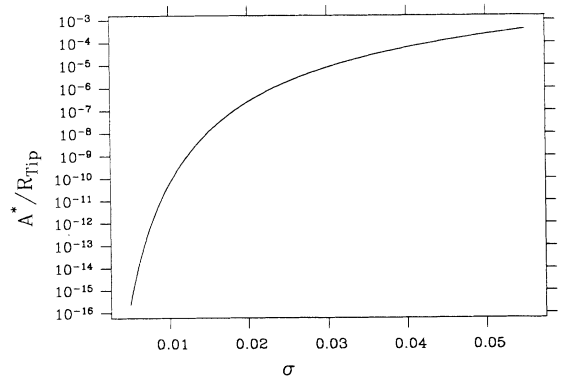


FIG. 13. Kinetic phase diagram of morphologies in the phase space of perturbation amplitude $A$ versus anisotropy parameter $\sigma$. The line shows the critical amplitude $A^*$ obtained from Eq. (15) with $c_1 = 1$. For amplitudes significantly smaller than $A^*$ the tip is stable; for significantly larger amplitudes the tip is unstable. Note the strong dependence of $A^*$ on $\sigma$ for small $\sigma$.

($l_D$ is the diffusion length) for a flat interface at $k=k^*$, where $\Omega$ has its maximum value. In Fig. 14 we show the action of such perturbations which apparently are above the critical threshold onto dendrites which consequently do not maintain compact dendritic form. Figure 14(b) is a typical snapshot of a fractal dendrite. Taking averages over such tip regions at various times analogously as done by Arneodo *et al.* [19] one arrives at an approximately parabolic envelope whose scaling is in agreement with the prediction for fractal dendrites [7].

Although the Mullins-Sekerka instability has only real eigenvalues a perturbation at the tip could at least in principle also oscillate in time with frequency $\omega$, thereby producing new spatial oscillations with new nodal points. Assuming conservation of the nodal points everywhere except at the tip—and ignoring external noise for the moment—it follows for small $\sigma$ that the oscillation period $\tau=2\pi/\omega$ is bounded by $\rho \gtrsim v\tau \gtrsim \lambda_s$. If such an oscillation in time of the perturbation exists, then it would be conceivable that the convective stabilization may not be sufficient to compensate for the still active Mullins-Sekerka instability mechanism and the tip might be linearly unstable. So far, however, we have no indication for such a process from our numerical studies.

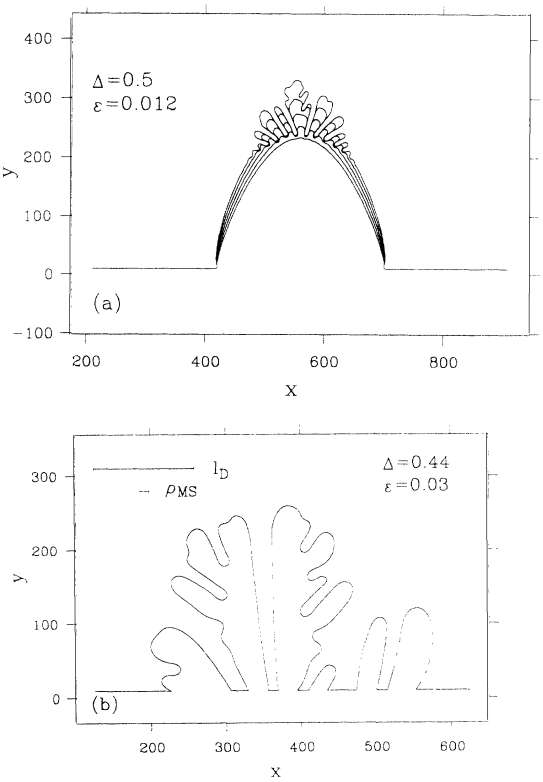


FIG. 14. (a) Evolution of a small perturbation of numerical origin at the tip. The stability length here was about $R_0/5$ with an initial tip radius $R_0=50$ and an initial diffusion length $l_D=267$. A well-defined spatially oscillating mode develops. The tip is unstable against this mode, which does not oscillate in time directly at the tip. As already mentioned in Fig. 9, here and in the following all lengths are measured in units of the computational lattice spacing $LU$. The parameters used were $D=1$, $\Delta=0.5$, $\epsilon_4=0.012$, and $d_0=0.0095$. (b) Fractal dendrite computed on four grids. The parameters used were $D=1$, $\Delta=0.44$, $\epsilon_4=0.03$, and $d_0=0.03$. The tip radius of the average envelope $R_{av}\approx 100$ is about a factor of 7 larger and the normalized average growth rate $V=v_{av}d_0=0.000\,45$ is a factor of 2 larger than the theoretical values for an ideal nonfractal dendrite without noise. The structure is a factor of 1.52 faster than the fractal seaweed pattern [Fig. 17(b)] with $\Delta=0.44$ and $\epsilon_4=0$. The scaling is in agreement with the theoretical prediction [7] for fractal dendrites.

## V. FRACTAL SEAWEED

A flat interface which separates a phase $A$ from a phase $B$ and which moves in a diffusion field at small supercooling cannot move indefinitely at a constant speed; otherwise global conservation of the diffusing species would be violated. In principle, however, a constant growth rate of an *average* interface is possible if behind that *average* interface the resulting "phase" is no more homogeneous but a mixture of the two phases $A$ and $B$. This means that the actual *local* interface between $A$ and $B$ must be meandering hereby forming alternating layers of phase $A$ and phase $B$. The envelope over this meandering two-phase region then is the average interface.

As a first central result of our simulations we describe here the formation of *fractal-seaweed* structures. They will be characterized by absence of observable anisotropies and second by the existence of a region of length scales within which a fractal dimension can be determined for the growing pattern. The theoretical scaling concept [7] is based on an earlier discovery [6] in Laplacian growth and can be summarized as follows. Assume that a scaling range for fractal structures exists between some short-range cutoff $\rho$ and the diffusion length $l_D$ so that the mass $m$ of the aggregated object scales with length $l$ as $m\sim(l/\rho)^{D_f}$, with $D_f$ as the fractal dimension. On scales larger than the diffusion length the object appears to have an average mass density $\eta<1$ and the mass scales simply as $m\sim\eta(l/\rho)^d$, with $d$ now being the actual dimension of space. Obviously, right at $l=l_D$ the two scaling relations must become equal

$$\left[\frac{l_D}{\rho}\right]^{D_f}\sim\eta\left[\frac{l_D}{\rho}\right]^{d}. \tag{19}$$

Assuming that the short-range cutoff $\rho$ is proportional to the stability length $\rho_{MS}=2\pi\sqrt{d_0 l_D}$, the equation allows for a determination of growth rate as a function of supercooling [7]. The evolution of patterns characterizable by this concept are now presented.

In Fig. 15 we show the time evolution of a hump initially introduced on the interface. The frame shown is always moved along with the forefront of the moving interface. In each of the little figures the moving interface moves upward into the channel, the sidewalls of the channel have mirror reflection boundary conditions for the diffusion field, and the top boundary is kept at the value for the infinitely distant diffusion field ahead of the moving interface. This top boundary is actually not shown here in order to save space. In all cases it is kept at least two diffusion lengths ahead of the topmost point

of the moving interface. The width of the channel here is more than five times the diffusion length. The final figure of this series already gives a clear indication for the existence of a fractal scaling range as the pattern shows some rather inhomogeneous distributions over space resembling cauliflower or seaweed.

In Fig. 16 we show the result of a box-counting analysis for the fractal dimension of the *boundary* of such a seaweed. The boundary curve was covered with a minimal number $N$ of circles of radius $R$. The measured length $L_R$ is then related to the fractal dimension $D_L$ of that surface by the obvious relation

$$L_R = NR \sim R^{-(D_L-1)}, \tag{20}$$

applicable in one of the limits $R \to \infty$ or $R \to 0$. Of course we can only expect some intermediate range between the two limits to follow such a scaling range: For smaller radii the structure becomes smooth $D_L = 1$ because of the smoothing effect of the surface tension, and at large radii screening effects are expected to become relevant. This is actually recovered in Fig. 16 where the slope of the curve corresponds to $-(D_L-1)$, giving $D_L \approx 1.67$. This value in fact is quite precisely equal to the value $\frac{5}{3}$ obtained by a mean-field argument for the *bulk* dimension.

The final state of the simulations for two different supercoolings $\Delta = 0.35$ and 0.44 and at zero anisotropy is shown in Fig. 17. Of course the structures still would be dynamically changing, but their characteristic quantities such as fractal dimensions have reached a steady state on average. The fractal structure becomes more obvious the smaller $\Delta$ is, as expected. The bulk fractal dimension $D_f$ can now be defined by a box-counting method in the usual way. Divide the system completely into squares of side length $r$. Any square containing a part of the bulk from the grown phase is counted as occupied. The number $N_r$ of occupied squares then should scale in the fractal region as

$$N_r \sim r^{-D_f} \tag{21}$$

at least over some range of $r$ values just like in the case of the fractal boundary discussed above.

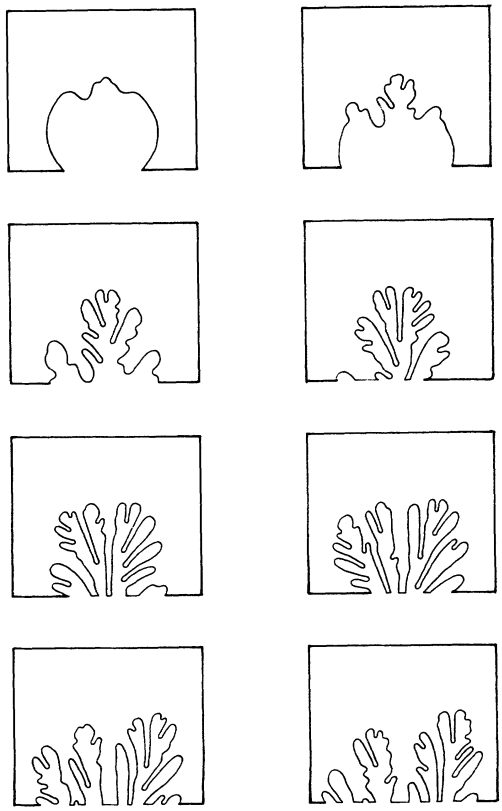

FIG. 15. Time evolution of a fractal seaweed structure with isotropic capillary length started from an initial hump. The parameters used were $D=1$, $\Delta=0.393$, channel width $W=700$, and $d_0=0.01$. The average velocity is about $v=0.016$, yielding a diffusion length $l_D=125$.

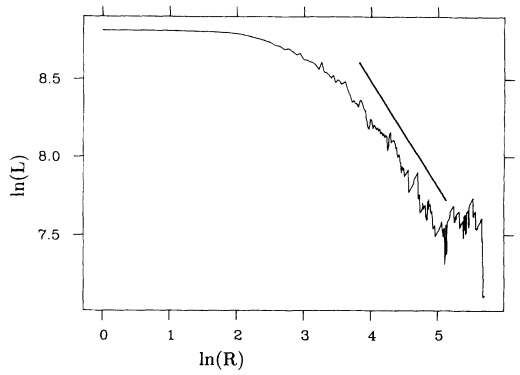


FIG. 16. The length $L$ of the whole solid-liquid boundary was measured by covering the interface with a minimum number of circles with radius $R$. The natural logarithm of $L$ is plotted vs the logarithm of $R$ in order to get the fractal dimension $D_L$ of the boundary from the slope $1-D_L$. This yields $D_L \approx 1.67$.

The result is plotted in Fig. 18. The box counting was restricted to be the central third of the channel width to minimize boundary effects. The effect is most pronounced for the smallest value of $\Delta = 0.35$ considered here. Shown is the effective fractal dimension $D_f(r)$ obtained from the evaluation of $D_f(r) = -\ln(N_{2r}/N_r)/\ln 2$ for two subsequent box divisions differing by a factor of 2 in box size. There clearly exists an intermediate range of length scales giving a plateau for the local fractal dimension at a value of about $D_f \lesssim 1.73$. At larger values of $\Delta$ the plateau is less pronounced and it lies at slightly larger values. Accordingly the result $D_f \leq 1.73$ must be considered as an upper bound and the surface exponent $D_L \approx 1.67 \leq D_f$ as a lower bound on the bulk fractal dimension. We conclude that our present result $1.67 \leq D_f \leq 1.73$ appears to be fully consistent with the value 1.715 found for the fractal dimension of Laplacian aggregation [21] in continuous space as was predicted [7].

The next point to be addressed concerns the scaling relation

$$v \sim \frac{D}{d_0}\Delta^{\psi}, \quad \psi = 2/(2-D_f), \tag{22}$$

predicted for the growth rate depending on supercooling for sufficiently small supercoolings. (We ignore possible

noise effects for the moment.) It originates from the relation mentioned above (19): $(l/\rho)^{D_f} \sim (l/\rho)^2\Delta$, where $l$ should be identified as the diffusion length and $\rho$ as the stability length, Eq. (7). From a log-log plot of the velocity vs $\Delta$ for the three values of $\Delta=0.35$, 0.393, and 0.44 we found that the three points clearly can be connected by a straight line with slope $\approx 6.0$. In order to show that this works well at least in this $\Delta$ range, we plot $V/\Delta^{\Psi}$ vs $\Delta$ in Fig. 19 with $\Psi=6.0$. The deviations from a horizontal straight line are within our numerical uncertainties. Assuming an exponent of $D_f \approx 1.71$, one would expect $\psi \approx 6.9$. On the other hand, if one would use a constant value of $\rho$ for the small scale cutoff independent of velocity as originally proposed and confirmed for stochastic growth model without surface tension [6], one would expect an exponent of about $\psi \approx 3.5$. Our results clearly support Eq. (22) with $\psi = 2/(2-D_f)$. These results therefore give a quantitative confirmation of this recently formulated scaling prediction [7]. Note also that it is by no means trivial that such an interface can move at a rate which is constant on average and not decreasing with time like a flat interface necessarily would do. The fractal scaling here is similar to scaling near a critical point in second-order phase transitions. The critical point would correspond to supercooling $\Delta \to 0$ so that the diffusion length diverges and the range of length scales corresponding to the plateau in Fig. 18 also diverges. Note that despite the fact that our smallest value of $\Delta=0.35$ still seems to be relatively large, the plateau in Fig. 18 extends over more than an order of magnitude in length scale already. In principle we could of course further reduce $\Delta$ in the simulations, but the large value of the exponent $\psi$ quickly leads to an enormous increase in the diffusion length as the long-range cutoff. This in turn would require a substantial increase in lattice size and computing time driving us quickly beyond the limits of currently available computer equipment. In any case the factor of 10 in length scales achieved here is apparently sufficient for a precision of the critical exponent $2/(2-D_f)$ within about 10%.

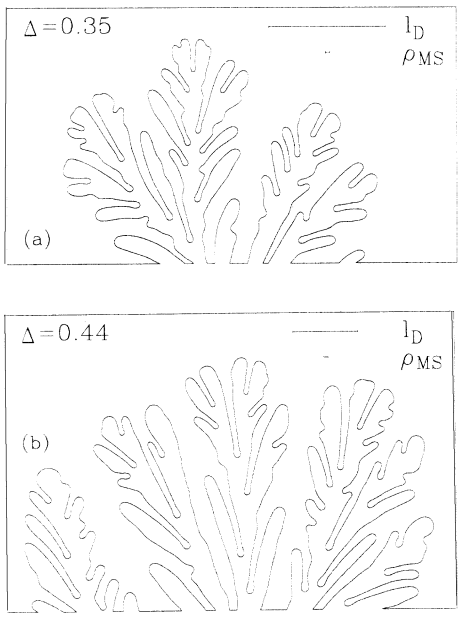


FIG. 17. Fractal seaweed structures grown over very long times in a wide channel (relative to the diffusion length $l_D$) at low undercooling. The average velocities of their envelopes have already reached constant values. The width of the narrow troughs is about equal to the Mullins-Sekerka length $\rho_{MS}$. The parameters used were $D=1$, $\epsilon_4=0$, and lattice size $1121\times1121$; (a) $\Delta=0.35$, $d_0=0.0068$, $l_D=182$, $\rho_{MS}=7$; (b) $\Delta=0.44$, $d_0=0.015$, $l_D=101$, $\rho_{MS}=7.7$. All lengths are given in lattice units $LU$ and all times in $LU^2/D$ are as already mentioned in Fig. 9.

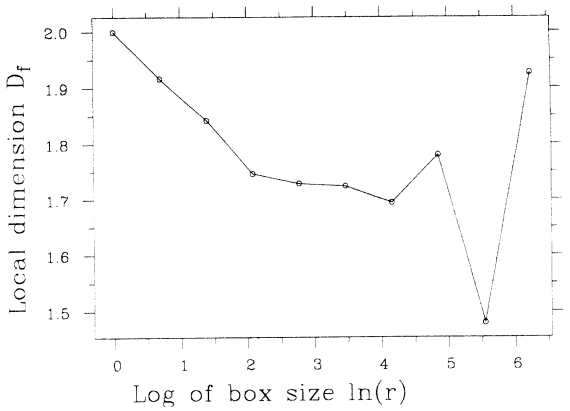


FIG. 18. Box-counting analysis of the pattern shown in Fig. 17(a). The central third of the channel is completely divided into squares of side length $r$. Any square containing a part of the bulk from the grown phase is counted as occupied. The number $N_r$ of occupied squares then should scale in the fractal region as $N_r \sim r^{-D_f}$. The local fractal dimension $D_f$, which should be independent of the box size $r$ for an ideal fractal, is plotted vs the natural logarithm of $r$. Here this is only true in a range of about one magnitude of length scales and gives a fractal dimension of $D_f \approx 1.73$. Symbols correspond to doubling of box size.

Finally we have also made an attempt to estimate the noise strength in these simulations and to test the prediction [7] of velocity depending logarithmically on noise as

$$v \sim \frac{D}{d_0} |\ln\Gamma|^{-2} \Delta^{2/(2-D_f)} . \tag{23}$$

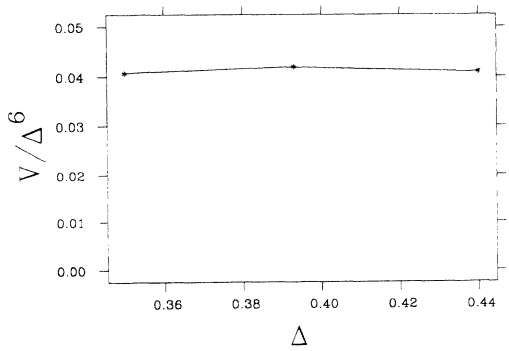


FIG. 19. The normalized average velocity $V=vd_0/D$ of the envelope of the structures from Fig. 17 and a structure at $\Delta=0.393$ (not shown) divided by $\Delta^{\Psi}$ with $\Psi=6.0$ is plotted vs undercooling $\Delta$. Deviations from a horizontal straight line are within our numerical uncertainty.

This comes from the prediction [7] of an extra length scale $\rho \sim |\ln\Gamma|\rho_{MS} > \rho_{MS}$ to appear in the Fourier spectrum of length scales in the systems shown in Fig. 17. We could not identify this extra scale. However, since everything is consistent with a noise strength of about order unity there is no contradiction, but also no independent support of the theory [7] from the results presented in this section. In any case the results on fluctuation effects in dendritic growth mentioned in Sec. IV confirm the predictions on noise dependence within the available precision.

## VI. COMPACT SEAWEED

The *compact-seaweed* morphology [7] was originally introduced on the basis of experimental observations under the name *dense branching* morphology [18]. At that time, however, its introduction as a morphological "phase" distinct from the well-known dendritic morphologies was completely speculative. Computer simulations also were inconclusive at that time. In addition there existed no indication that an interface in an isotropic medium could advance at a steady growth rate under diffusion control if the dimensionless supercooling was different from unity.

The first indication for the existence of such a distinct phase came (to our knowledge) from arguments [7] based on a theoretical study of crystal growth in a channel [37]. This analysis of channel growth gave among other things the following results. A finger-type pattern symmetrically in the center of the channel could grow at constant growth rate for dimensionless supercoolings $\Delta > 0.5$. The finger looks similar to the Saffmann-Taylor finger [38] of viscous flow, but belongs to a different branch of the mathematical solution. The growth rate of the crystal increases with increasing driving force $\Delta$, as to be expected. A specifically remarkable result of this theory [37] is that the driving force sets a length scale and thereby also a velocity: For a given driving force $0.5 < \Delta < 1$ there exists a characteristic channel width below which such a steadily growing finger is no longer possible (length here in units of the capillary length). If one increases the channel width $w$ from this critical value the growth rate $v$ of the

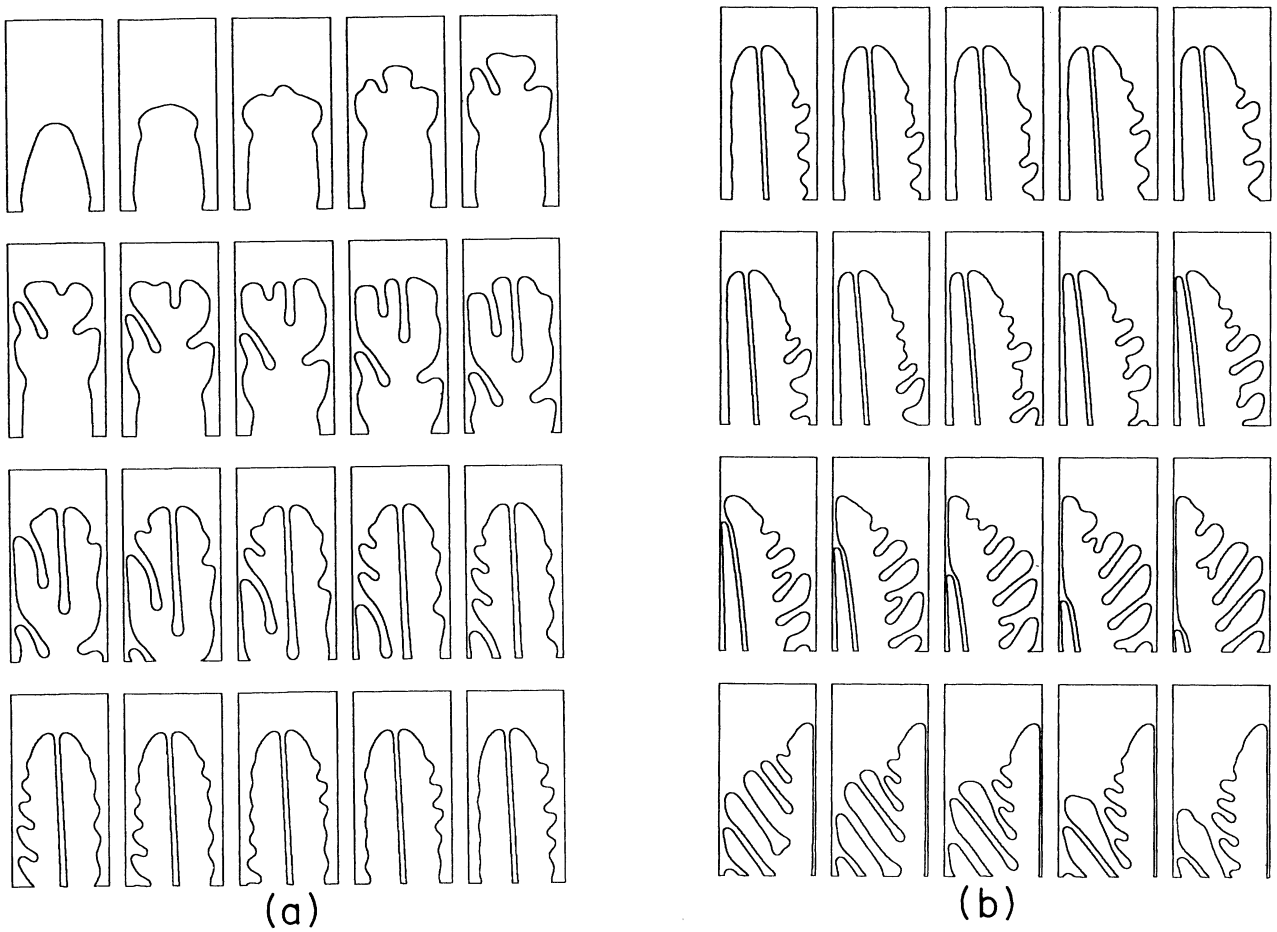


FIG. 20. Evolution of a nonsymmetrical finger in a wide channel of width $W = 800d_0 = 300$ lattice units with $D = 1$, $\Delta = 0.7$, $\epsilon_4 = 0$, $d_0 = 0.375$, $l_D = 38$, $R_{tip} = 17.9$, and the small gap between finger and wall is 7.139. Note the long existence of a pair of two nonsymmetrical fingers. The growth rate is selected essentially independent of the channel width $W$. The sidebranches occur at the same wavelength as on an anisotropic dendrite growing at the same velocity. Because the two walls of the channel are numerically not identical, the mirror image of the structure and the related diffusion field were taken as new initial conditions, as indicated in the last five frames. The pattern became stationary as before with a velocity only 1% smaller. This is a consistency test both for the pattern as for the numerical code.

resulting finger first increases, goes through a maximum, and then decreases again as $v \sim w^{-1}$ (with the diffusion constant as a proportionality factor). For wide channels this is consistent with the condition imposed by the conservation law that the diffusion length cannot be substantially smaller than the width of the finger. Otherwise the phase separation occurring during finger formation by diffusion could not take place.

In a previous numerical investigation by a Green's-function technique [39] this predicted behavior was confirmed for channel growth. We have now repeated these simulations with our fully dynamical code and confirm the cited results. In particular we also quantitatively confirm the appearance of a *symmetry-broken* (SB) finger which grows off center in the channel once a critical width has been exceeded (Fig. 28). In a previous study [39] on channel growth we could not decide whether this occurrence of the asymmetrical finger is a linear or a nonlinear instability. This will be discussed in more detail at the end of this section.

These asymmetric or symmetry-broken fingers seem to represent a key point in the growth of compact-seaweed morphology as already mentioned [17]. In Fig. 20 we show a practically dendritic SB finger moving along the wall as it develops with time from some initially centered perturbation in a channel with reflecting sidewalls. Its tip radius and growth rate matches within 1% with the

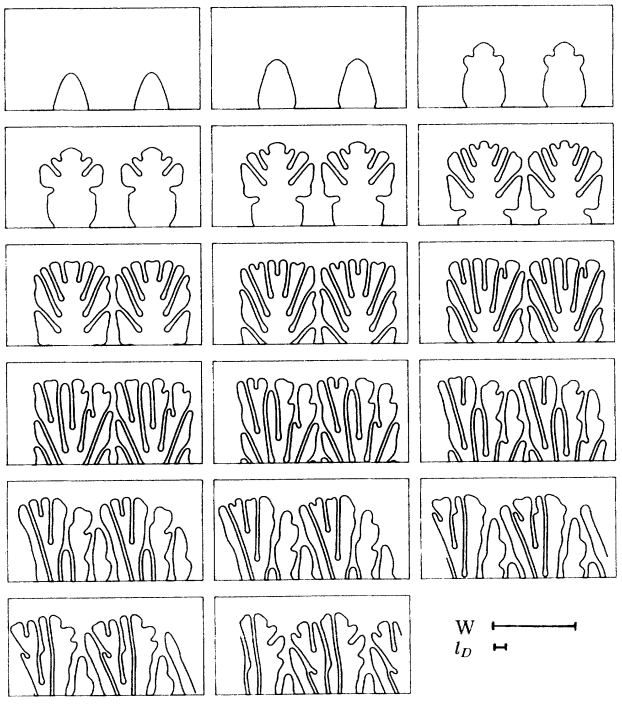


FIG. 21. Time sequence of channel growth with periodic boundary conditions at the walls. Here two periods are plotted. Structures like the asymmetric fingers in Fig. 20 start to dominate this compact seaweed pattern. The first pictures look like unstable dendrites, which is probably due to some rest anisotropy, because we used only two grids for the simulation. The parameters used were $D=1$, $\Delta=0.7$, $\epsilon_4=0$, lattice size $851\times851$, $d_0=0.434$, and $W=478$. The average velocity was $v_{av}=0.04$, which gives $l_D=50$.

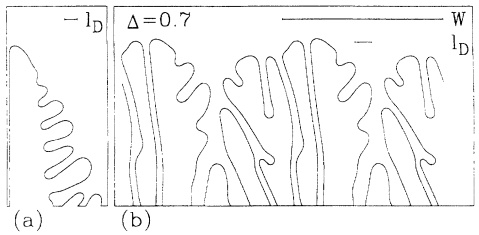


FIG. 22. (a) Final state of the time sequence from Fig. 20 (not shown there). (b) Last picture of the compact seaweed structure shown in Fig. 21. Structures like the asymmetric fingers in (a) are visible. The diffusion length is only about 10% of the periodicity length $W$. The growth rate is only 15% slower than in (a). This supports the idea [7] of a growth rate selection mechanism intrinsic to the pattern.

results obtained by the Green's-function method in quasistationary approximation [39]. In Fig. 21 we show the corresponding time sequence, but now with periodic boundary conditions, i.e., without walls on the sides of the channel. Surprisingly it looks as if the resulting seaweed pattern tries to form asymmetric double fingers in order to mimic the existence of a reflecting wall. We assert the convergence to stationary growth rate apart from spatiotemporal fluctuations. This is also obvious in the comparison given in Fig. 22 (with and without wall; see our previous abbreviated paper [17]).

It seems that the resulting finger structure may depend also on initial conditions as seen in Fig. 23 where two differently developed asymmetrical fingers run in parallel over several diffusion lengths. The finger tips, however, do not depend on details. In Figs. 24(a) and 24(b) we again show two snapshots of a double finger evolving with time under periodic boundary conditions. Figure 24(b) has essentially come to a final state of steady motion. The finger grows at an angle of 8.7° against the average vertical growth direction. Would some remaining 16-fold anisotropy be responsible for this angle (on four rotated lattices) one should expect an angle of 22.5° or 12.25°. We have rotated this pattern into vertical

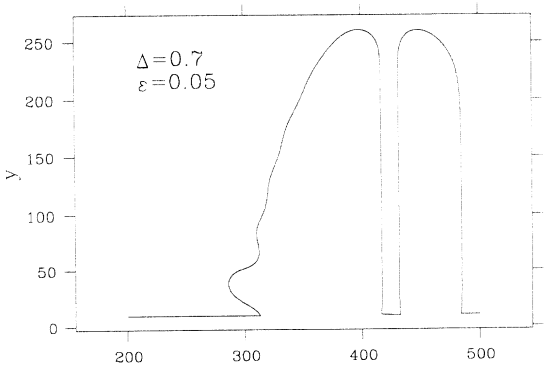


FIG. 23. Two different developed SB fingers running parallel in a channel with reflecting walls at small anisotropy $\epsilon_4=0.05$. We obtained this structure by starting with a parabola with $\epsilon_4=0$ and switching on anisotropy after the first tip splitting. The parameters and observables used were $D=1$, $\Delta=0.7$, $d_0=0.375$, $l_D=34$, and $R_{tip}=17.3$.

direction and it moves on without any substantial change as shown in Fig. 24(c). For comparison we have here superimposed a finger growing along a wall (together with its mirror image) grown at the same physical parameters. The quantitative agreement is striking. The tip radius on the foremost points of these fingers, the distance between the double fingers, and the growth rates agree within 2%. These double fingers appear to act like solitons (or better, "doublons"), since they seem to be stable against fluctuations and, even more surprisingly, against decomposition. Therefore we think that the growth in a channel in fact bears the answer also to the free growth of compact seaweed as predicted [7], even though we cannot give a precise analytical solution for these symmetry-broken fingers at present.

Note that this demonstrates that an isotropic compact seaweed exists at constant growth rate. Note also that this compact seaweed moves faster than a dendritic pattern, Fig. 25, if the capillary anisotropy needed to define the dendrites is smaller than some critical value, about $\epsilon_4 \approx 0.12$ for $\Delta = 0.7$. This shows that the compact seaweed is a growth morphology qualitatively different from the dendritic morphology and dominant at sufficiently small anisotropies. This indicates a discontinuous phase transition to occur as we will discuss later. The growth in the compact-seaweed region accordingly should be controlled by a small number of such doublons such that we cannot exclude that the pattern overall looks rather similar to the compact-dendritic growth mode.

The SB double fingers with anisotropy were obtained by using the SB fingers without anisotropy as initial condition, while the dendrites have grown from a parabola. The only difference is the initial condition. With increasing anisotropy the gap between the two fingers becomes wider and the velocity and radius of the tip come closer to the corresponding values for free dendritic growth. If the anisotropy reaches a critical value $\epsilon_{crit} \approx 0.12$, the pair solution becomes unstable. The two fingers drift very slowly away from each other undergoing some kind

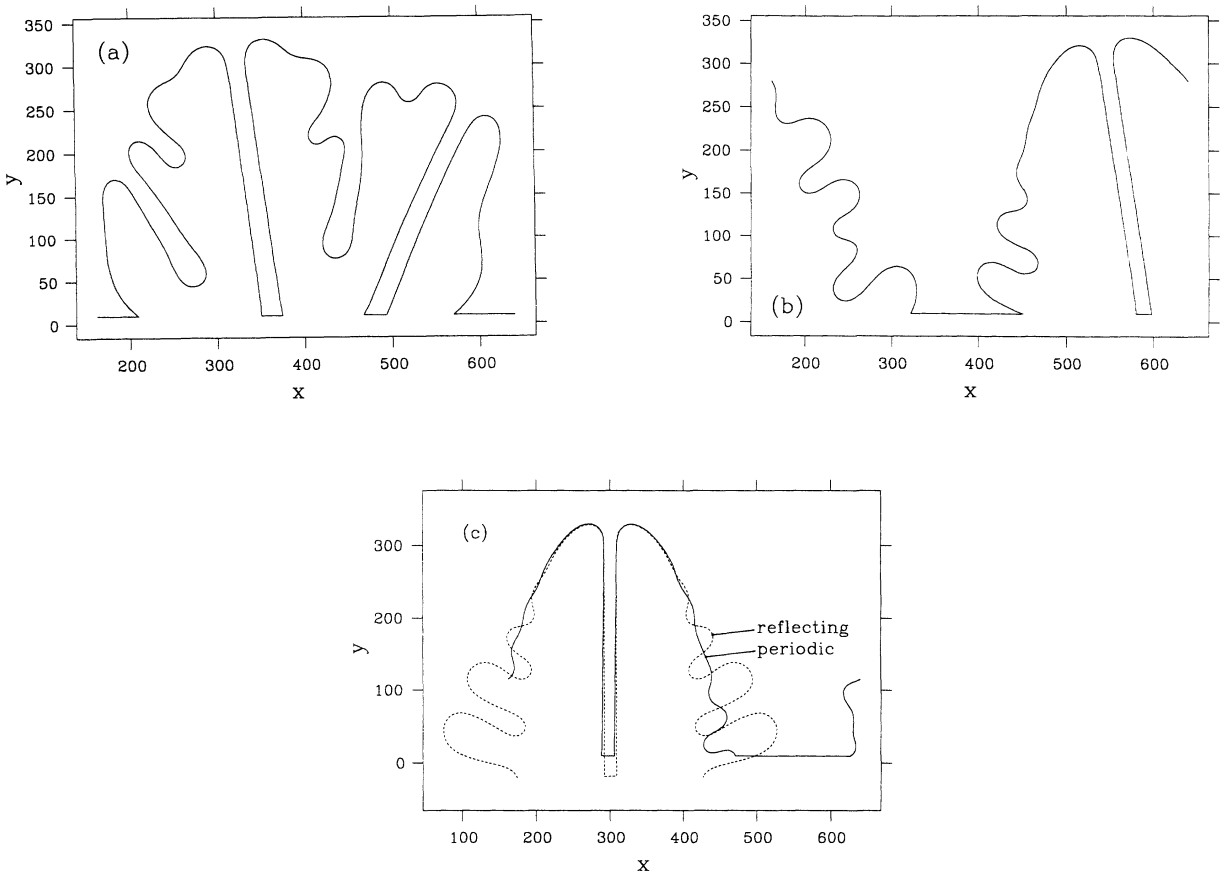


FIG. 24. Channel growth with periodic boundaries on the sides with exactly the same parameters as in Fig. 21 simulated on four grids over long times. No walls exist on the sides. (a) Corresponds to a rather early snapshot of the pattern, while (b) has essentially converged to the final structure. In (b) there is only one pair of SB fingers growing with a constant rate into a direction with an angle $\alpha \approx 8.7°$ to the periodic boundaries. This angle depends on the initial conditions. This pattern (b) was rotated into vertical direction. (c) Shows this rotated structure after growing over ten diffusion lengths. Note that there is no substantial change of the shape of the pattern. $R_{tip} = 22.5$, $v = 0.0441$, and the gap between the fingers is 17.0. Furthermore we have superimposed onto this free double finger a finger from Fig. 20 growing along a wall together with its mirror image. This shows that the free double finger is very similar to an asymmetric finger close to a wall. As already mentioned, all lengths are given in lattice units $LU$, all times in $LU^2/D$, and all velocities in $D/LU$.

of unbinding transition in order to become single dendrites. This drift cannot be an initial relaxation because it is still visible after growing over 85 diffusion lengths, Fig. 26. Note also the increase in width compared to Fig. 25. Furthermore we checked at anisotropy zero that these nonsymmetrical fingers exist also for smaller undercoolings $\Delta=0.68,0.64$ with lower velocity and larger tip radius, but at $\Delta=0.62$ the tip is destroyed by noise-induced sidebranching similar to the fractal dendritic case. This is in contrast to the doublon-unbinding described before. Although we are not quite sure yet that the unsymmetrical solution vanishes completely below some critical $\Delta_{crit}$, this supports the distinction between two phases below (fractal seaweed) and above $\Delta_{crit}\approx 0.6$ (compact seaweed) at the present level of noise. A clear distinction of the two phases on the basis of the predicted different internal length scales of the two morphologies would require an approach to $\Delta\approx 0.5$ at substantially reduced noise which we could not achieve so far. Assuming a critical value of $\Delta_{crit}=0.5$ to exist as a limit for the CS region as predicted, both the velocity and the tip radius of the nonsymmetrical finger scale in the range $0.64\leq\Delta\leq 0.75$, in quite good agreement with the prediction [Eq. (11) of Ref. [7]).

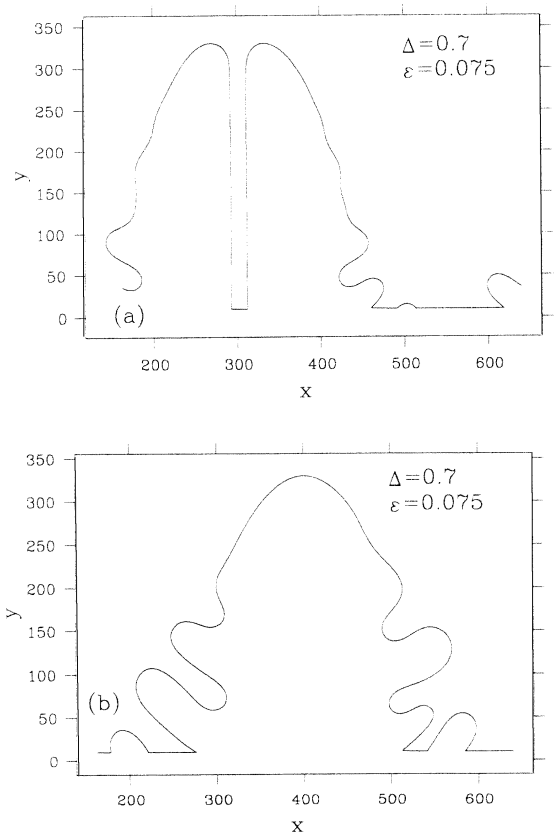


FIG. 25. (a) SB fingers with anisotropy $\epsilon=0.075$. The fingers with isotropic surface tension as shown in Fig. 24(c) are used as initial conditions. All other parameters, except anisotropy, are the same as in Fig. 24: $R_{tip}=19.9$ and $v=0.0515$. (b) A normal dendrite with the same physical and numerical parameters as in (a), but with a parabola as initial condition. Apparently there are two kinds of stable solutions. The dendrite moves slower than the SB fingers by a factor of about 1.6. $R_{tip}=37.1$ and $v=0.0332$.

In Fig 27 we give the growth velocity versus capillary anisotropy for the two possible branches of solutions observed in these simulations, compact seaweed and compact dendritic patterns. As mentioned already before [17] this is a direct indication for the existence of a discontinuous phase transition between the two growth morphologies. Previous simulations on related models did not show the independent existence of the two morphologies at the same parameters.

A general argument that the transition should be of first order is that a critical point generally is of codimension-two, so that two parameters must be adjusted in order to reach the transition point. In other words, if in a system described by two parameters $(\Delta,\epsilon)$ only one parameter is varied $(\epsilon)$ and the other is kept fixed at an arbitrary value, the phase transition is typically of first order. This assumption is also supported by a recent analytical check [40] that the transition from the symmetrical finger in a channel with reflecting walls [37] to a symmetrical dendrite is of first order. Concerning the symmetry-breaking transition we show in Fig. 28 the transition from a symmetrical (free) dendrite to an asymmetrical dendrite moving along the wall in a relatively narrow channel with reflecting sidewalls. The control parameter which was varied here was the anisotropy.

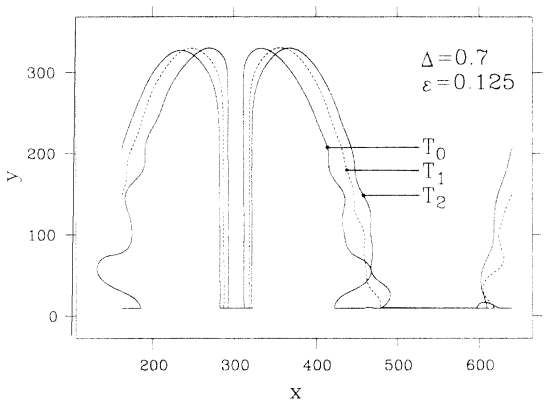


FIG. 26. An unstable pair of SB fingers at $\epsilon_4=0.125$ grown on four grids with periodic boundaries. The structure with $\epsilon_4=0.075$ of Fig. 25(a) was used as initial condition. No other parameters were changed. The fingers drift slowly away from each other in order to become free dendrites. Note that this drift is no initial relaxation process, because the structure has already grown by about 85 diffusion lengths at time $T_2$. The parameters used were $D=1$, $\Delta=0.7$, $d_0=0.4345$, $R_{tip}=19.4$, $l_D=34.5$, and growth time $T_0=0$, $T_1=25\,900$, and $T_2=49\,490$. At time $T_2$ the tip radius and the velocity have reached quite constant values of $R_{tip}=19.4$ and $v=0.058$. The values of the corresponding free dendrite, which was simulated with the same parameters but with the dendrite with $\epsilon_4=0.075$ as initial condition [Fig. 25(b)], are $R_{tip}=20.1$ and $v=0.0571$. There is only a difference of about 3% to the values of the two drifting fingers. Furthermore there is a distance of about 3.9 diffusion lengths between the tips of the two fingers as seen in the figure. Hence we can conclude that these fingers have already become free dendrites.

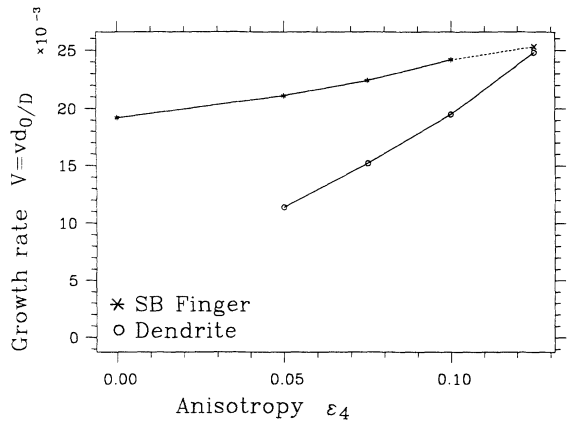


FIG. 27. Normalized velocity $V=vd_0/D$ vs anisotropy of $\epsilon_4$ for SB fingers (upper curve, $*$) and dendrites (lower curve, $\circ$). The channel has periodic boundary conditions and all parameters are as in Figs. 21, 24, and 25. If one approaches the critical anisotropy (here $\epsilon_{crit} \lesssim 0.125$) from below, the distance between the two SB fingers increases and their velocity and tip radius come closer to the values of the corresponding dendrite. At anisotropy 0.125 there is no stable pair solution; the two fingers tend away from each other very slowly in order to become free dendrites. The crossover region from SB fingers to dendrites is given by the dashed line. Up to now it is not clear whether the two lines for dendrites and SB fingers are really connected. The point $\times$ corresponds to the two dendrites of Fig. 26.

While in Fig. 25(b) the dendritic solution is obtained in a system with periodic boundary conditions without a wall, the walls in Fig. 28 allow the dendrite to break the symmetry and, together with its mirror image across the wall, to develop a double-finger structure. This appears to be precisely what happens in the wide system without a wall, Figs. 24 and 25 that two fingers move as twins in a double-finger structure.

We think that this symmetry-breaking transition in a

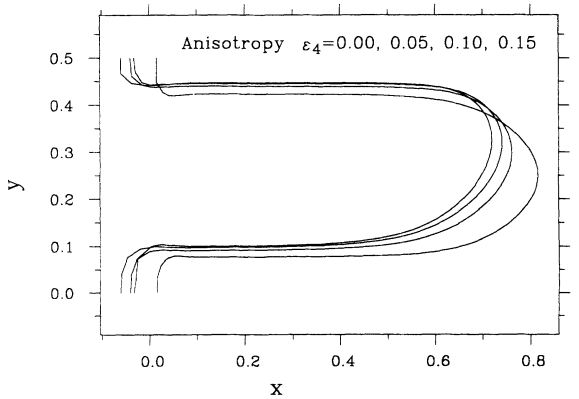


FIG. 28. Structure of symmetrical and symmetry-broken fingers in a channel at parameters $\Delta=0.7$, $d_0=0.01$, $W=200d_0$, and anisotropy $\epsilon_4=0.00, 0.05, 0.10, 0.15$ obtained with the Green's-function method from [16,39]. We checked that the calculation at $\epsilon_4=0$ with the fully time-dependent method agrees within 3%. The width $W$ of the channel is just above the critical value where nonsymmetrical solutions can occur [39]. At anisotropy 0.15 the finger is in the center of the channel (position 0.25 on vertical axis), with decreasing anisotropy the position becomes off center. Reflecting walls are at positions $y=0.0$ and 0.5.

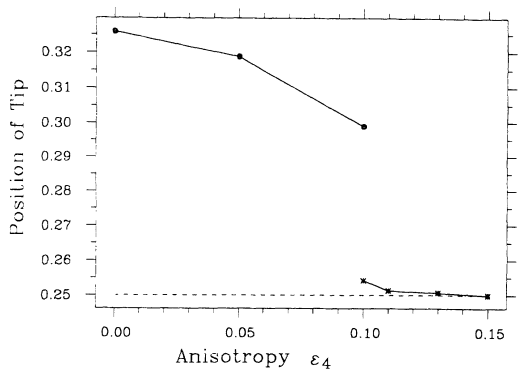


FIG. 29. Position of the finger tip in the channel of Fig. 28 plotted versus anisotropy. The walls are at position values of $y=0.0$ and 0.5, respectively. A position near $y=0.25$ corresponds to a symmetrical finger. A transition to an asymmetrical finger takes place when the anisotropy becomes smaller than 0.11. At $\epsilon_4=0.10$ both a symmetrical and unsymmetrical finger can grow as a stationary metastable pattern. This shows that the transition is discontinuous.

wide channel with reflecting walls is the same as the pairing-unpairing transition Fig. 26 in the free system. We have studied this in somewhat more detail using the Green's-function method [39] employed previously for channel growth. A central result of this analysis is shown in Fig. 29 for supercooling $\Delta=0.7$ giving the position of the finger as a function of anisotropy. Note that the channel has here a width of 0.5 in internal units, corresponding to 200 times the capillary length $d_0$. The center of the channel accordingly is at position 0.25. For anisotropies larger than about $\epsilon_4=0.1$ the finger can remain in the center and for smaller anisotropies a position closer to the wall is also possible. Note in particular that at anisotropy $\epsilon=0.1$ both positions, near the center or near the wall, are possible for the same set of parameters. This proves that the transition from the center to the wall under reduction of anisotropy is of *first order* or *discontinuous*, because in the neighborhood of the transition two solutions can exist in a state which is at least metastable. The small deviations visible from the central position

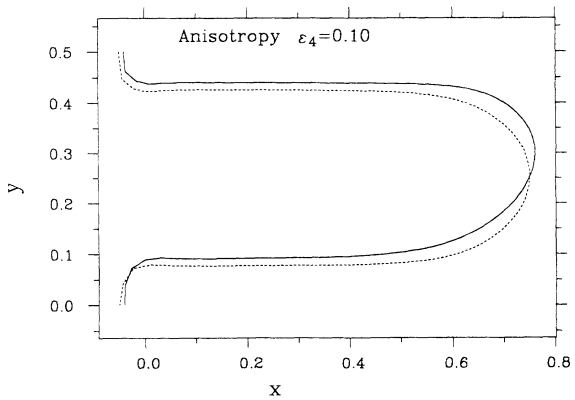


FIG. 30. Symmetrical and asymmetrical finger for the same anisotropy $\epsilon_4=0.1$. Other parameters were the same as in Fig. 28. The global conservation as expressed in the finger width is fulfilled with a relative precision of about $10^{-3}$ for both patterns.

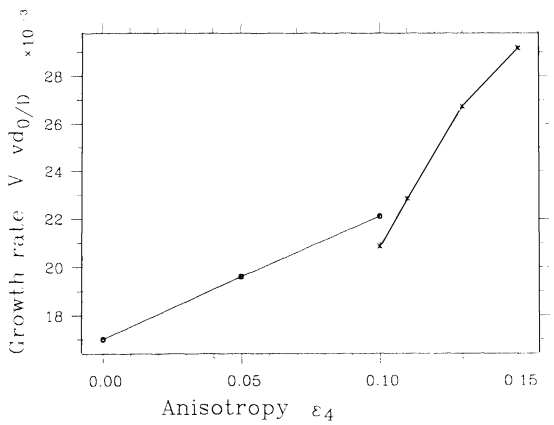


FIG. 31. Velocity of the finger in the channel with reflecting boundaries as in Figs. 28 and 29 plotted versus anisotropy. The left branch corresponds to the asymmetrical finger and the right branch at larger anisotropies to the symmetrical finger. It is still not clear whether the asymmetrical branch stops before it reaches the symmetrical branch around $\epsilon_4 \approx 0.11$ or whether the two branches intersect. Note the similarity to Fig. 27, where in contrast periodic boundary conditions were used and the channel was about five times wider. For further details see text.

near the position values of 0.25 in Fig. 29 are due to small numerical symmetry-breaking effects such as the channel not being centered around the numerical value of zero. Since they are irrelevant for all of the conclusions we did not remove them. In addition this proves here the metastability of the solution at the center. A comparison of these two fingers at $\epsilon_4 = 0.1$ is shown in Fig. 30. Finally we show in Fig. 31 the resulting velocities as a function of anisotropy. Again these are clearly two different branches for the symmetrical and for the asymmetrical finger. (Note that Fig. 31 looks very similar to Fig. 27.) We have tried to increase the anisotropy from 0.10 to 0.11 for the anisotropic finger, but after a very long relaxation the finger converged to the symmetrical solution. Therefore, we cannot decide at present whether the asymmetrical branch intersects the symmetrical branch in the velocity vs anisotropy relation.

This suggests some interesting possibilities for the pattern selection process. The two branches plotted in Figs. 29 and 31 show that two different velocities are possible around anisotropy of 0.1. One may assign different measures of stability or resilience to these two patterns according to whether the system under noise spends more time around the one or the other of the two structures. It seems to be by no means clear that the pattern which is more stable or more resilient in this sense also is the one which runs with higher growth velocity. If the more resilient pattern is the faster one, it will be the one selected, but if it would be the slower one, then it depends on the product of these two measures which of the patterns would cover a large percentage of space at long times. While the results of Figs. 29 and 31 were obtained for a still rather narrow channel, we expect that they hold also qualitatively unchanged for the wide channel and finally for the infinite system with respect to the double-finger transition. We expect, furthermore, that for a sufficiently narrow channel (but still wider than the critical width [37,39]) the transition could change from a discontinuous into a continuous transition with the analog of a tricritical point in between. We will leave this together with a more detailed analysis of the velocity dependence near the transition point to a forthcoming investigation.

## VII. CONCLUSION

We presented a numerical method to study the advancement of an interface due to diffusional transport. It was shown that the effects of the artificial anisotropy due to the computational lattice can be suppressed by using a stack of rotated lattices. The basic predictions for the occurrence of the growth morphologies compact and fractal dendrites for anisotropic surface tension and compact and fractal seaweed for vanishing anisotropy were confirmed. We found that for arbitrary driving forces an average interface can move at constant growth velocity even with fully isotropic surface tension. Furthermore we found fractal seaweed structures at zero anisotropy and small driving forces $\Delta \lesssim 0.5$ with a fractal dimension $1.66 \leq D_f \leq 1.73$, in agreement with the case of simple Laplace aggregation without surface tension as predicted [7]. If the anisotropy is increased the pattern can be described as fractal dendritic, growing faster than a compact dendrite, which is obtained at larger anisotropy. This is in agreement with the prediction for noisy dendrites. At large driving force $\Delta \gtrsim 0.5$, we see a transition from the compact dendritic to the compact seaweed morphology when anisotropy is reduced. Symmetry-broken fingers of the growing phase seem to be the basic building blocks for the compact-seaweed morphology. These results are supported by studies on channel growth which give a discontinuous transition from the dendritic to the channel (seaweed) mode of growth. Within our numerical accuracy the velocities become equal at the transition point, but there is still another possibility not completely ruled out yet. A major point to be clarified finally is still the quantitative influence of noise on these pattern-selection processes and we hope to report on this in the near future.

## ACKNOWLEDGMENTS

We thank E. Brener, K. Kassner, Y. Saito, and D. Temkin for many valuable discussions. This work was partly supported by a grant from the GIF, and we also thank E. Ben-Jacob, S. Lipson, and O. Shochet for valuable discussions.

[1] K. Kawasaki, M. Suzuki, and A. Onuki, *Formation, Dynamics, and Statistics of Patterns* (World Scientific, Singapore, 1990).
[2] J. S. Langer, Rev. Mod. Phys **52**, 1 (1980).
[3] L. I. Rubinstein, *The Stefan Problem* (American Mathematical Society, Providence, RI, 1971).
[4] W. Mullins and R. Sekerka, J. Appl. Phys. **34**, 323 (1963).
[5] H. Müller-Krumbhaar and W. Kurz, in *Phase Transfor-*

*mation in Materials,* edited by P. Haasen (VCH-Verlag, Weinheim, 1991).
[6] M. Uwaha and Y. Saito, Phys. Rev. A **40**, 4716 (1989).
[7] E. Brener, H. Müller-Krumbhaar, and D. Temkin, Europhys. Lett. **17**, 535 (1992).
[8] S. C. Huang and M. E. Glicksman, Acta. Metall. **29**, 701 (1982); **29**, 707 (1982).
[9] J. Bechhoefer and A. Libchaber, Phys. Rev. Lett. **35**, 1393 (1987); J. Bechhoefer, A. J. Simon, J. Libchaber, and P. Oswald, Phys. Rev. A **39**, 3974 (1989).
[10] P. Oswald, J. Malthete, and P. Pelce, J. Phys. (Paris) **50**, 2121 (1989).
[11] P. Oswald, J. Bechhoefer, and F. Melo, MRS Bull. **16**, 38 (1991).
[12] J. S. Langer, in *Chance and Matter,* edited by J. Souletie, J. Vannimenus, and R. Stora (Elsevier, Amsterdam, 1987).
[13] D. A. Kessler, J. Koplik, and H. Levine, Adv. Phys. **37**, 255 (1988).
[14] E. A. Brener and V. I. Mel'nikov, Adv. Phys. **40**, 53 (1991).
[15] Y. Pomeau and M. Ben Amar, in *Solids Far From Equilibrium,* edited by C. Goldréche (Cambridge University Press, Cambridge, England, 1992).
[16] Y Saito, G. Goldbeck-Wood, and H. Müller-Krumbhaar, Phys. Rev. Lett. **58**, 1541 (1987); Phys. Rev. A **38**, 2148 (1988).
[17] T. Ihle and H. Müller-Krumbhaar, Phys. Rev. Lett. **70**, 3083 (1993).
[18] E. Ben-Jacob, G. Deutscher, P. Garik, N. Goldenfeld, and Y. Lereah, Phys. Rev. Lett. **57**, 1903 (1986).
[19] O. Shochet, K. Kassner, E. Ben-Jacob, S. G. Lipson, and H. Müller-Krumbhaar, Physica A **181**, 136 (1992); **187**, 87 (1992).
[20] A. Arneodo, Y. Couder, G. Grasseau, V. Hakim, and M. Rabaud, Phys. Rev. Lett. **63**, 984 (1989); A. Arneodo, F. Argoul, Y. Couder, and M. Rabaud, *ibid.* **66**, 2332 (1991).
[21] T. A. Witten and L. M. Sander, Phys. Rev. Lett. **47**, 1400 (1981); Phys. Rev. B **27**, 5686 (1983).
[22] E. Brener, T. Ihle, H. Müller-Krumbhaar, Y. Saito, and K. Shiraishi, Physica A (to be published).
[23] G. P. Ivantsov, Dokl. Akad. Nauk. SSSR **58**, 567 (1947).
[24] J. S. Langer and H. Müller-Krumbhaar, Acta. Metall. **26**, 1681 (1978); **26**, 1689 (1978); **26**, 1697 (1978); H. Müller-Krumbhaar and J. S. Langer, *ibid.* **29**, 145 (1981).
[25] F. Liu and N. Goldenfeld, Phys. Rev. A **42**, 895 (1990).
[26] R. Almgren, J. Comput. Phys. **106**, 337 (1993).
[27] A. A. Wheeler, B. T. Murray, and R. J. Schaefer, Physica D **66**, 243 (1993).
[28] R. Kobayashi, Physica D **63**, 410 (1993).
[29] J. A. Sethian and J. Strain, J. Comput. Phys. **98**, 231 (1992).
[30] D. A. Kessler and H. Levine, Phys. Rev. Lett. **57**, 3069 (1986).
[31] M. Barber, A. Barbieri, and J. S. Langer, Phys. Rev. A **36**, 3340 (1987); J. S. Langer, *ibid.* **36**, 3350 (1987).
[32] B. Caroli, C. Caroli, and B. Roulet, J. Phys. (Paris) **43**, 1423 (1987).
[33] R. Pieters and J. S. Langer, Phys. Rev. Lett. **56**, 1948 (1986).
[34] W. v. Saarloos, B. Caroli, and C. Caroli, J. Phys. I (Paris) **3**, 741 (1993).
[35] D. Bensimon, Phys. Rev. A **33**, 1302 (1986); A. J. DeGregoria and L. W. Schwartz, J. Fluid. Mech. **164**, 383 (1986); D. A. Kessler and H. Levine, Phys. Rev. A **33**, 2621 (1986); **33**, 2634 (1986).
[36] Y. Saito and K. Shiraishi, in *Spatio-Temporal Patterns in Nonequilibrium Complex Systems, NATO Advanced Study Institute, Series B: Physics,* edited by P. E. Cladis and P. Palffy-Muhoray (Plenum, New York, in press).
[37] E. Brener, M. Geilikman, and D. Temkin, Zh. Eksp. Teor. Fiz. **94**, 241 (1988) [Sov. Phys. JETP **67**, 1002 (1988)].
[38] P. Saffman and G. Taylor, Proc. R. Soc. London Ser. A **245**, 312 (1958).
[39] E. Brener, H. Müller-Krumbhaar, Y. Saito, and D. Temkin, Phys. Rev. E **47**, 1151 (1993).
[40] E. Brener and D. Temkin (private communication).